Global and Planetary Change 229 (2023) 104236

Contents lists available at ScienceDirect

Global and Planetary Change

journal homepage: www.elsevier.com/locate/gloplacha

# Driver of eustatic change during the early Aptian Oceanic Anoxic Event 1a (~120 Ma)

Yiwei Xu [a,b], Xiumian Hu [b,*], Eduardo Garzanti [c], Gaoyuan Sun [d], Jingxin Jiang [b], Juan Li [a], Shijie Zhang [e], Felix Schlagintweit [f]

[a] State Key Laboratory of Palaeobiology and Stratigraphy, Nanjing Institute of Geology and Palaeontology and Center for Excellence in Life and Paleoenvironment, Chinese Academy of Sciences, Nanjing 210008, China
[b] State Key Laboratory of Mineral Deposits Research, School of Earth Sciences and Engineering, Nanjing University, Nanjing 210023, China
[c] Department of Earth and Environmental Sciences, Università di Milano-Bicocca, Milano 20126, Italy
[d] College of Oceanography, Hohai University, Nanjing 210098, China
[e] College of Tourism, Henan Normal University, Xinxiang 453000, China
[f] Lerchenauerstr. 167, Munich 80935, Germany

ARTICLE INFO

Editor: Dr. Alan Haywood

*Keywords:*
Eustasy
OAE1a
Carbonate platform
Iran
Dariyan Formation

ABSTRACT

Sea-level changes exert an important control on oceanic circulation and climate evolution. Researchers have proposed that sea-level rise favored accumulation of sediments enriched in organic carbon during oceanic anoxic events (OAEs), although high-frequency sea-level changes and their controlling mechanism have remained poorly constrained. Here we present a detailed sedimentological and geochemical study on Aptian (Lower Cretaceous) shallow-water carbonates of the Dariyan Formation exposed in the Zagros fold belt of southern Iran. Microfacies analysis reveals that a regression occurred during carbon isotopic stages C3-C4, followed by a transgression during stages C6-C7. Frequency analysis of carbonate allochems indicates a transition from rudists and other skeletal grains to microbial grains with reduced bioturbation during regression at late C3-C5 stages, whereas the opposite occurred during transgression at stages C6-C7. In the transition interval (C3-C5) nutrients (P, Ba) and redox indicators (Ce anomaly and U concentration) document low nutrient levels and oxygen-rich sea waters, suggesting sea-level changes, rather than by seawater chemistry control. Worldwide correlation of relative sea-level changes across Tethyan, Northern Atlantic, Pacific and Arctic areas is consistent with regression followed by transgression during OAE1a. The regression and transgression occurred at a period of climatic warming and cooling respectively, suggesting that aquifer-eustasy rather than thermo-eustasy or glacio-eustasy may have represented the main cause of eustatic changes.

## 1. Introduction

Global sea-level is observed to rise today at a rate of ~3.7 mm per year (Fox-Kemper et al., 2021), profoundly influencing all communities living in coastal to shallow-marine settings, modifying the land/ocean distribution, and affecting oceanic circulation and climate change (Zhang et al., 2023). Eustatic rise also determines the expansion of oxygen-depleted conditions in epicontinental seas (Grötsch et al., 1998; Bond and Wignall, 2008; Hermoso et al., 2013) and influences marine biodiversity (Brett et al., 2007; Ludt and Rocha, 2015; Bartlett et al., 2018).

The mid-Cretaceous world was characterized by a prolonged warm climate punctuated by several transient oceanic anoxic events (OAEs) with widespread deposition of black shales (Jenkyns, 2010). Event OAE1a (Selli Level of the Umbria-Marche Apennines) took place in the early Aptian (~120 Ma), a relatively cold period when small ice caps may have been present in the polar area (Wang et al., 2011; Herrle et al., 2015; Alley et al., 2019). Associated with OAE1a were nannofossil crisis (Erba et al., 2010), increased seawater temperature (Naafs and Pancost, 2016; Jenkyns, 2018), intensified continental weathering (Bottini et al., 2012; Lechler et al., 2015), and the demise of carbonate platforms (Weissert et al., 1998; Huck et al., 2011).

The sedimentary evolution during OAE1a has been widely associated with eustatic rise, leading to accumulation of organic carbon-rich

* Corresponding author.
*E-mail address:* huxm@nju.edu.cn (X. Hu).

https://doi.org/10.1016/j.gloplacha.2023.104236
Received 4 May 2023; Received in revised form 22 August 2023; Accepted 4 September 2023
Available online 9 September 2023

sediment and drowning of carbonate platforms (Föllmi et al., 1994; Weissert et al., 1998; Grötsch et al., 1998; Millán et al., 2009; Huck et al., 2011). The detailed pattern of sea-level change, however, remained poorly understood for several reasons. Firstly, organic-carbon content cannot be used as a proxy for sea-level rise, because oxygen depletion in seawater and increased primary production also takes place during OAEs (Föllmi et al., 1994; Bodin et al., 2013; Westermann et al., 2013; Erba et al., 2015). Secondly, most drowned carbonate platforms are located along the northern margin of Neotethys (e.g., Huck et al., 2014; Núñez-Useche et al., 2020), drowning unconformities are commonly multiphase, and some preceded the OAE1a event (Huck et al., 2011; Najarro et al., 2011; Masse and Fenerci-Masse, 2013; Frau et al., 2020). Thirdly, most evidence of sea-level change during OAE1a is based on condensed deep-marine successions, which prevents an accurate reconstruction of high-frequency sea-level changes.

In this study, we present an integrated sedimentological, biostratigraphic, microfacies, geochemical, and carbon-isotope analysis of shallow-water carbonates of the Dariyan Formation exposed in the Zagros fold belt of southern Iran. Our main aims are to: (1) improve our understanding of the evolution of carbonate platforms along the southern margin of the Neotethys Ocean; (2) reconstruct a detailed regional record of sea-level changes during OAE1a; (3) test the validity of the simple eustatic-rise model in a well-studied shallow-marine carbonate setting.

## 2. Geological setting

The Dariyan Formation (belonging to the Bangestan Group) consists of a carbonate platform deposited at subtropical latitudes along the northern passive continental margin of Arabia during the late Early Cretaceous (Fig. 1A and B). During the Aptian, the Kazhdumi and Bab basins developed in the platform interiors, reaching water depths of 50–100 m (Fig. 1B; Murris, 1980; van Buchem et al., 2010a) and remaining as the only marine areas during the late Aptian regression when the Dariyan platform was widely exposed (Ziegler, 2001; van Buchem et al., 2010a; Raven et al., 2010). The Khormoj stratigraphic

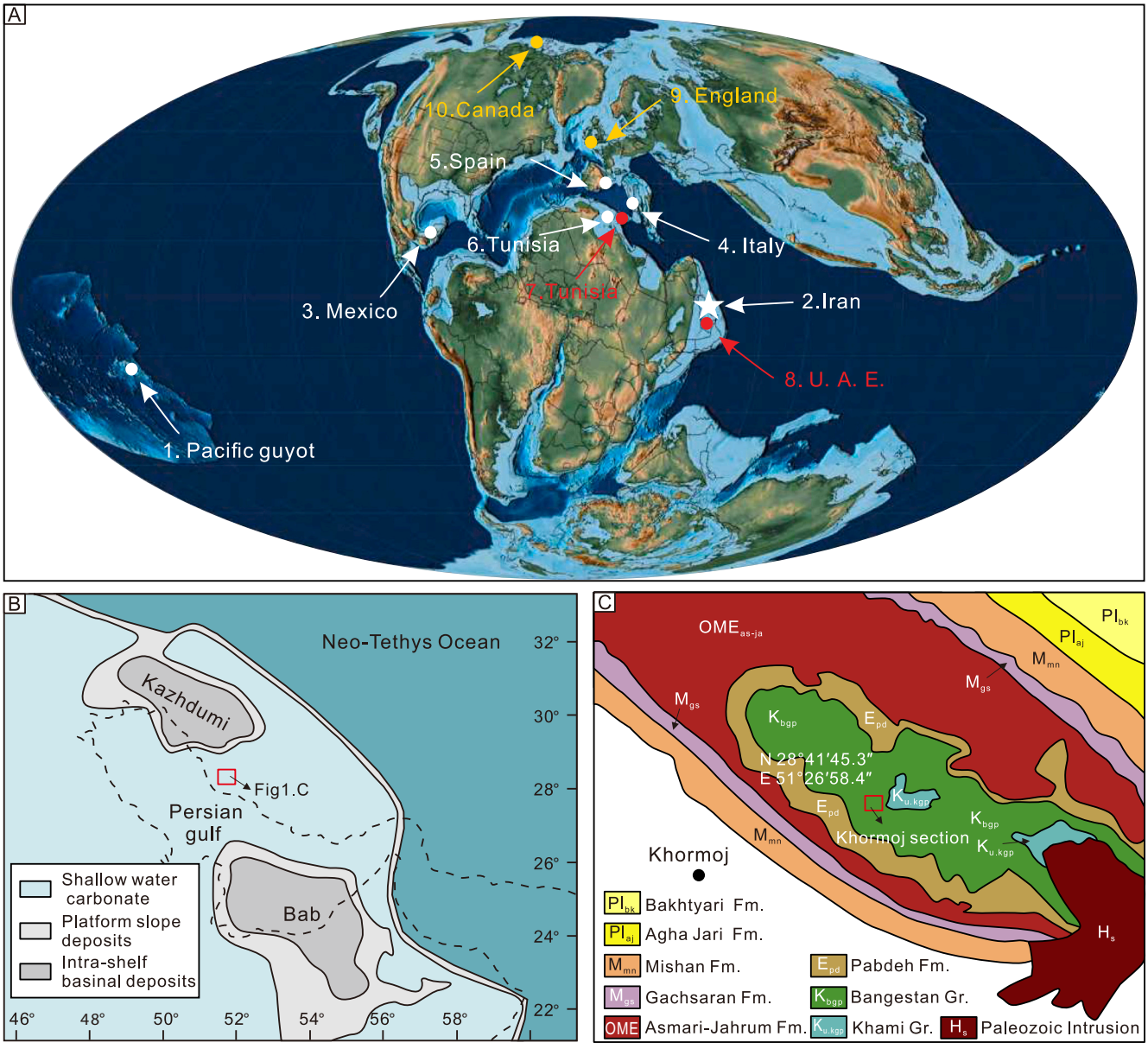


**Fig. 1.** A) Early Aptian paleogeographic map indicating paleoposition of key OAE1a localities discussed in text (after Scotese, 2021). Section: #1–6: neritic carbonates (#2 is Khormoj section), #7–8 pelagic limestones, and #9–10 siliciclastic deposits; B) Early Aptian paleogeography of the Arabian shelf (redrawn from van Buchem et al., 2010a); C) geological map of the Khormoj area (redrawn from Homke et al., 2009).

section analyzed in detail in the present study is situated on the platform adjacent to the Kazhdumi basin, where only lower Aptian platform deposits are documented (Fig. 1C).

The Aptian age of the Dariyan Formation is based on Sr isotopes and biostratigraphy (van Buchem et al., 2011; Afghah and Haghighi, 2014; Naderi-Khujin et al., 2016). In the studied area, the OAE1a interval has been well identified in previous works, which also documented OAE1a-related layers with *Lithocodium–Bacinella* facies (Vincent et al., 2010; Naderi-Khujin et al., 2016). The carbon-isotope curve of the Khormoj section showed a prominent positive excursion related to OAE1a (Vincent et al., 2010), although poor biostratigraphic control made such a correlation tentative. The lower Dariyan Formation in the Khormoj section chiefly consists of orbitolinid limestone and shows a deepening-upward trend, whereas a shallowing-upward trend characterizes the upper Dariyan Formation (Vincent et al., 2010; van Buchem et al., 2010b).

This study focuses on the ~85 m-thick upper Dariyan Formation, starting with a ~ 26-m-thick bioturbated limestone with rudist debris (Fig. 2A) intercalated with an in situ rudist biostrome (Fig. 2B) and followed by ~14-m-thick, thin- to medium-bedded limestone lacking bioturbation (Fig. 2C). The overlying 34-m-thick limestones with *Thalassinoides* (Fig. 2D) are followed in turn by a 12-m-thick rudist biostrome (Fig. 2E, F) capped by a 1-m-thick orbitolinid-rich limestone (Fig. 2E) displaying a hardground with borings on the top surface (Fig. 2G). A paleosol separates the Dariyan Formation from the overlying Burgan sandstone (Fig. 2E), indicating exposure and karstification during a major relative sea-level fall (van Buchem et al., 2010a).

## 3. Methods

### 3.1. Sampling and microfacies analysis

The Khormoj section is exposed to the northeast of Khormoj city (N 28°41′45.3″; E 51°26′58.4″) along the flanks of an anticline including Jurassic (Khami Group), Cretaceous (Bangestan Group) and Cenozoic strata (Pabdeh, Asmari, Jahrum, Gachsaran, Mishan, Agha Jari, and Bakhtyari formations) (Fig. 1B). This study focuses on the upper part of the Dariyan Formation, where samples were collected with an average spacing of 1–2 m. A total of 45 thin sections were used for microfacies analysis based on grain components, textures, and fossil assemblages. Carbonate rocks were classified based on Dunham (1962) and Embry and Klovan (1971). Frequency analysis was carried out by counting between 150 and 250 carbonate grains (depending on sample heterogeneity) using grain-bulk measurements (Flügel, 2010) with software *JMicroVision* (Roduit, 2019).

### 3.2. Stable carbon and oxygen isotopes

A total of 45 isotope analyses on bulk samples were performed at the State Key Laboratory for Mineral Deposits Research at Nanjing University using an in-line GasBench II auto sampler coupled to a Thermo Finnigan MAT Delta Plus XP mass spectrometer. Powdered samples were


**Fig. 2.** Outcrop photographs of the Khormoj section (southern Iran). A) Thick-bedded bioclastic limestones at the base of measured section; B) well-preserved rudist biostrome; C) thin-bedded limestones with small macrofossils; D) *Thalassinoides* in the upper part of section; E) top of Dariyan Formation represented by a rudist biostrome overlain by an orbitolinid-rich layer separated from the Burgan sandstone by a paleosoil; F) close-up view of rudist biostrome at top of Dariyan Formation; G) hardground on top of orbitolinid-rich layer.

obtained by microdrilling with a tungsten carbide drill bit, taking care to avoid cement-filled veins, pores and bioclasts, and reacted with purified orthophosphoric acid at 70 °C. Isotopic measurements were calibrated to Chinese national standard calcium carbonate sample GBW04405 ($\delta^{13}C_{VPDB}$ 0.57‰ ± 0.03‰; $\delta^{18}O_{VPDB}$ -8.49‰ ± 0.14‰). Isotope ratios are expressed in standard delta notation (δ) as per mil deviations relative to the Vienna Pee Dee Belemnite (VPDB) standard. The analytical precision (1σ) was better than 0.1‰ for $\delta^{13}C$ and 0.05‰ based on duplicate measurements of standards and samples. Carbon and oxygen isotope data are provided in Table S1.

### 3.3. Major and trace elements

Approximately 50 mg of powdered carbonate-rock samples were weighed and left to dissolve overnight in 3 ml of distilled 0.5 M acetic acid, after which the insoluble residues were weighed. The solutions were centrifuged, and the supernatant was transferred to another beaker. The residues were rinsed three times using ultrapure water, and the solutions were added to the previous supernatant. The leachates were converted to nitric acid medium, which was used for elemental analysis carried out at Nanjing Institute of Geology and Palaeontology, Chinese Academy of Sciences. Trace-element concentrations were determined using an Agilent 7700A inductively coupled plasma mass spectrometer (ICP–MS) with analytical precision better than ±2%. Major elements were measured using an Agilent 710 ICP–OES with analytical precision better than ±5%.

The cerium anomaly (Ce/Ce*) is calculated based on the relative depletion or enrichment in PAAS- (Post-Archean Australian Shale; Taylor and McLennan, 1985) normalized Ce ([Ce]SN) against neighboring nonredox-sensitive rare earth elements (REE), using the equation $Ce/Ce^* = Ce/(Pr \times (Pr/Nd))$ of Lawrence et al. (2006). Geochemical data for carbonate are provided in Table S2.

## 4. Results

### 4.1. Biostratigraphy

Abundant benthic foraminifers preserved in the Khormoj section of the upper Dariyan Formation were correlated to the orbitolinid biozones revised by Schroeder et al. (2010). The distribution of typical orbitolinid species are shown in Fig. 3. From samples 19KJ12 to 19KJ28, the occurrence of *Palorbitolina lenticularis* indicates the *P. lenticularis* zone of earliest Aptian age (Fig. 4A, C). The coexistence of *P. lenticularis* and *Palorbitolinoides pileus* above sample 19KJ29 (Fig. 4B) indicates a late early Aptian age and the occurrence of *Praeorbitolina cormyi-wienandsi* above sample 19KJ42 indicates the latest early Aptian. The two stratigraphic intervals between samples 19KJ29 and 19KJ41 and between samples 19KJ42 and 19KJ46 correlate to the Tethyan ammonite zones *Deshayesites deshayesi* and *Dufrenoya furcate,* respectively (Schroeder et al., 2010). Biostratigraphic evidence thus testifies to an early Aptian age for the studied Khormoj section, with the onset of OAE1a occurring beneath the first appearance of *Praeorbitolina cormyi-wienandsi* (i.e., beneath sample 19KJ42).

### 4.2. Carbonate microfacies and environmental changes

Based on field observations, sedimentological features, fossil assemblages, textures and fabrics, 13 microfacies (MF1 to MF13) grouped

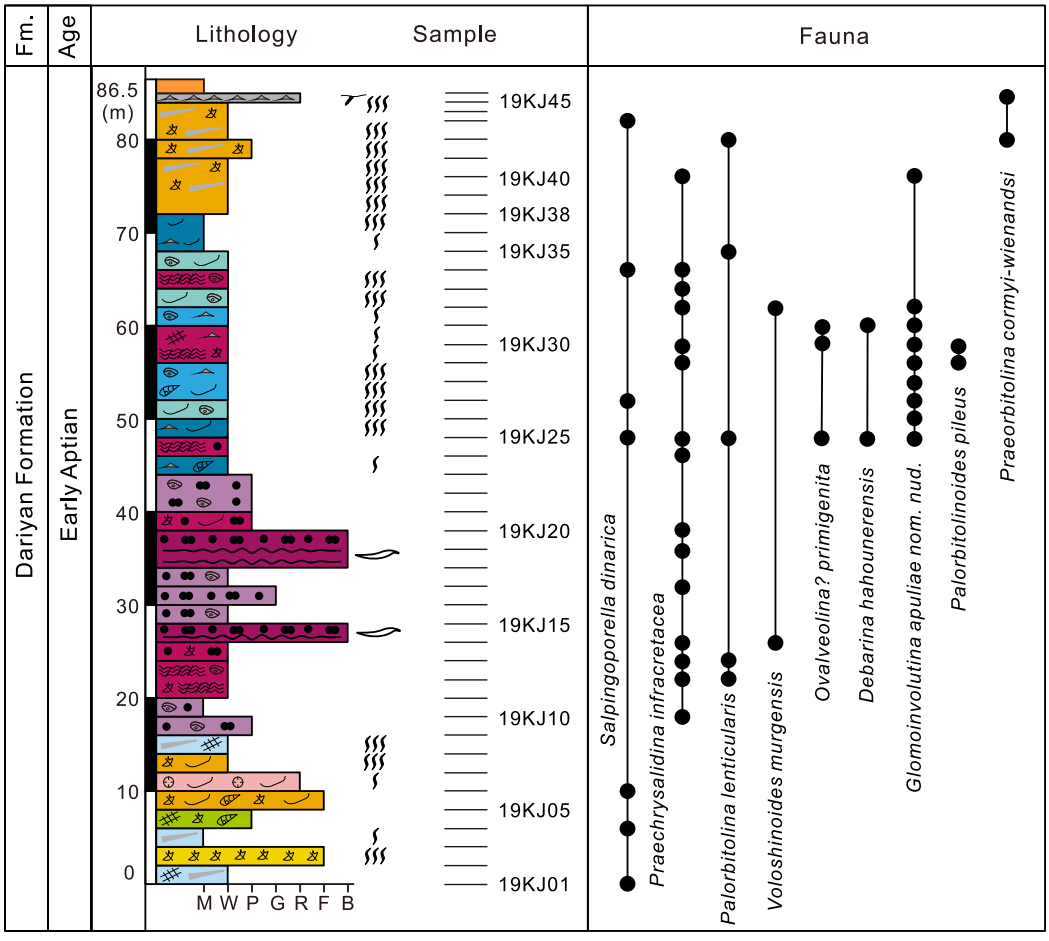


**Fig. 3.** Distribution of key foraminiferal speices throughout the Khormoj section (southern Iran). Legend as in Fig. 6.

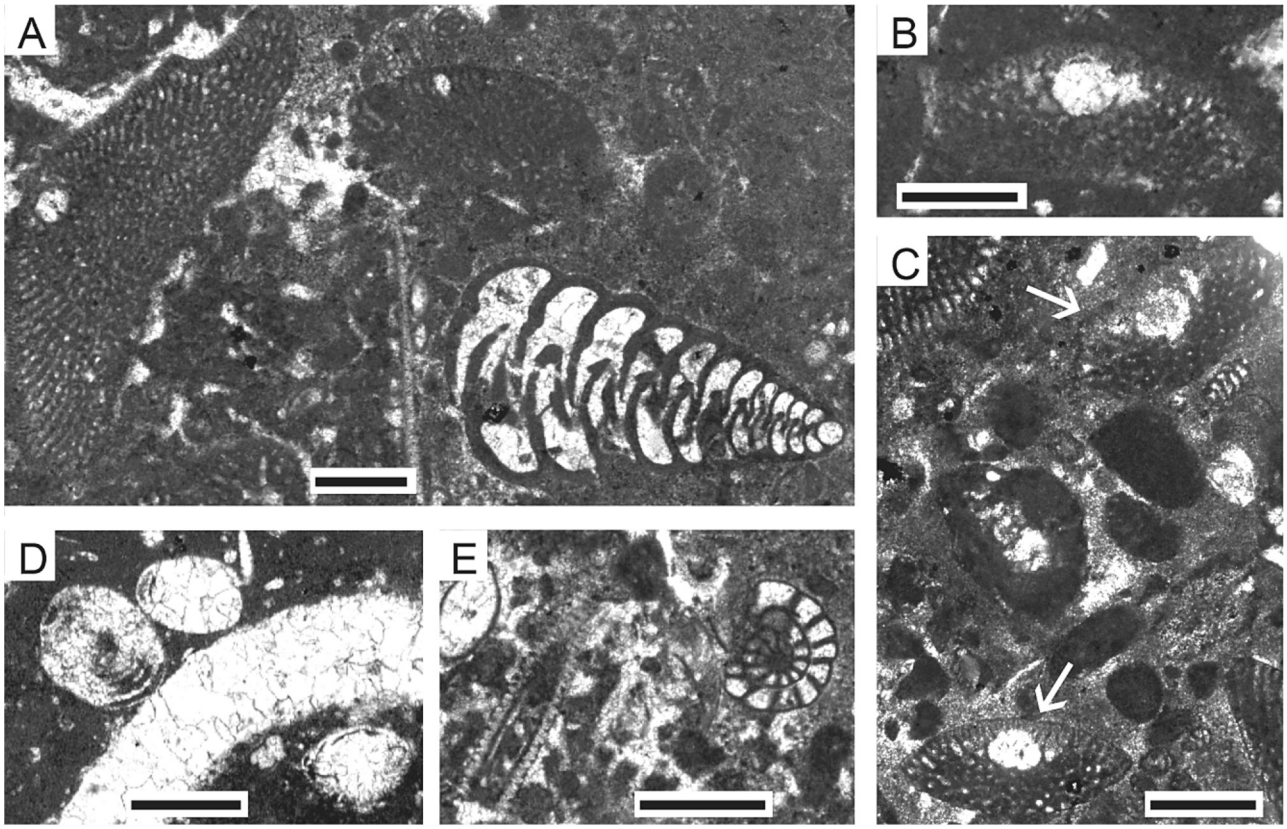


**Fig. 4.** A) *Palorbitolina lenticularis* (Blumenbach) (left) and *Praechrysalidina infracretacea* Luperto Sinni (right), sample 19KJ12; B) *Palorbitolinoides pileus* sensu Schroeder et al. (2010), sample 19KJ30; C) Two specimens of *Palorbitolina lenticularis* (Blumenbach) (arrows), sample 19KJ26; D) Three specimens of '*Glomoinvolutina apuliae*' Luperto Sinni and Masse nom. nud., sample 19KJ27; E) *Salpingoporella dinarica* Radoičić (left) and *Nezzazata* sp. (right), sample 19KJ12. Scale bars all 0.5 mm.

into four depositional settings were identified in the Khormoj section.

#### 4.2.1. Deep subtidal environment

*4.2.1.1. MF1 Orbitolinids rudstone-floatstone.* Thin-bedded limestones in the uppermost part of the Dariyan Formation are characterized by abundant (16–55%) and well preserved flat orbitolinids set in a micritic matrix (Fig. 5A). Bivalves and echinoderms occur; small miliolids and sponge spicules are rare. Flat orbitolinids are more common than conical forms in environments with turbid water, greater water depth, and low illumination (Vilas et al., 1995). Intense bioturbation and a hardground (Fig. 2G) indicate very slow deposition during relative sea-level rise (Flügel, 2010). Microfacies MF1, directly overlying the rudist biostrome, points to a deep subtidal environment below fair-weather wave base.

*4.2.1.2. MF2 Bioclastic wackestone-mudstone.* Thin- to medium-bedded limestone in the middle to upper part of the Khormoj section contain diversified bioclasts (flat orbitolinids, crinoids, bivalves, gastropods, sponge spicules, and small benthic foraminifers) set in micritic matrix (Fig. 5B). Bioturbation (e.g., *Thalassinoides*, commonly occurring in sublittoral environments; MacEachern et al., 2007) occurs on stratal surfaces (Fig. 2D).

Diversified fauna suggests an open marine environment; abundant micrite and sparse bioclasts indicate deep subtidal low-energy conditions.

*4.2.1.3. MF3 Spicule wackestone with algae.* Strata with abundant siliceous sponge spicules set in micritic matrix occur at the base of the Khormoj section (Fig. 5C). Strongly broken bivalves and green algae are common; *Hensonella* (considered to be either a dasycladacean alga or a *problematicum*) and small benthic foraminifers are rare. Siliceous sponges thrive in relatively deep water (Flügel, 2010) and association with MF4 indicates a deep subtidal environment.

*4.2.1.4. MF4 Bimodal rudist floatstone.* Thick-bedded, extensively bioturbated limestones at the base of the Khormoj section largely consist of coarse and poorly sorted rudist debris, with bioclasts ranging 0.3–5 mm in diameter, lacking micrite envelopes, and set in micritic matrix (Fig. 5D). Benthic foraminifers are rare. Diagenetic dolomitization was observed. Poorly-sorted rudist debris and lack of micrite envelope point at storm-induced events followed by rapid burial in a deep subtidal environment below fair-weather wave base (Flügel, 2010).

*4.2.1.5. MF5 Bioclastic packstone.* Thick-bedded limestones at the base of the Khormoj section contain abundant, well sorted, broken, and recrystallized bioclasts (mainly bivalves and green algae) set in micritic matrix (Fig. 5E). Some bioclasts display micrite envelopes. Rudists and *Hensonella* are minor. Microfacies MF5, interbedded with MF3 and overlain by an in situ rudist biostrome (Fig. 2B), point at high-energy, storm-induced events and deposition in a deep subtidal environment.

*4.2.1.6. MF6 Coral rudstone.* Thick-bedded limestones in the lower part of the Khormoj section mainly (~50%) consist of clasts of bored corals (1.5–3 cm in diameter, Fig. 5F) with minor (~5%) rudists and other bivalve debris. Flat orbitolinids, gastropods, *Hensonella*, echinoderms, and sponge spicules occur. During the mid-Cretaceous, corals thrived in deeper water than rudists (Gili et al., 1995; Fernández-Mendiola et al., 2013), indicating that microfacies MF6, interbedded with MF7, represents a deep subtidal environment.

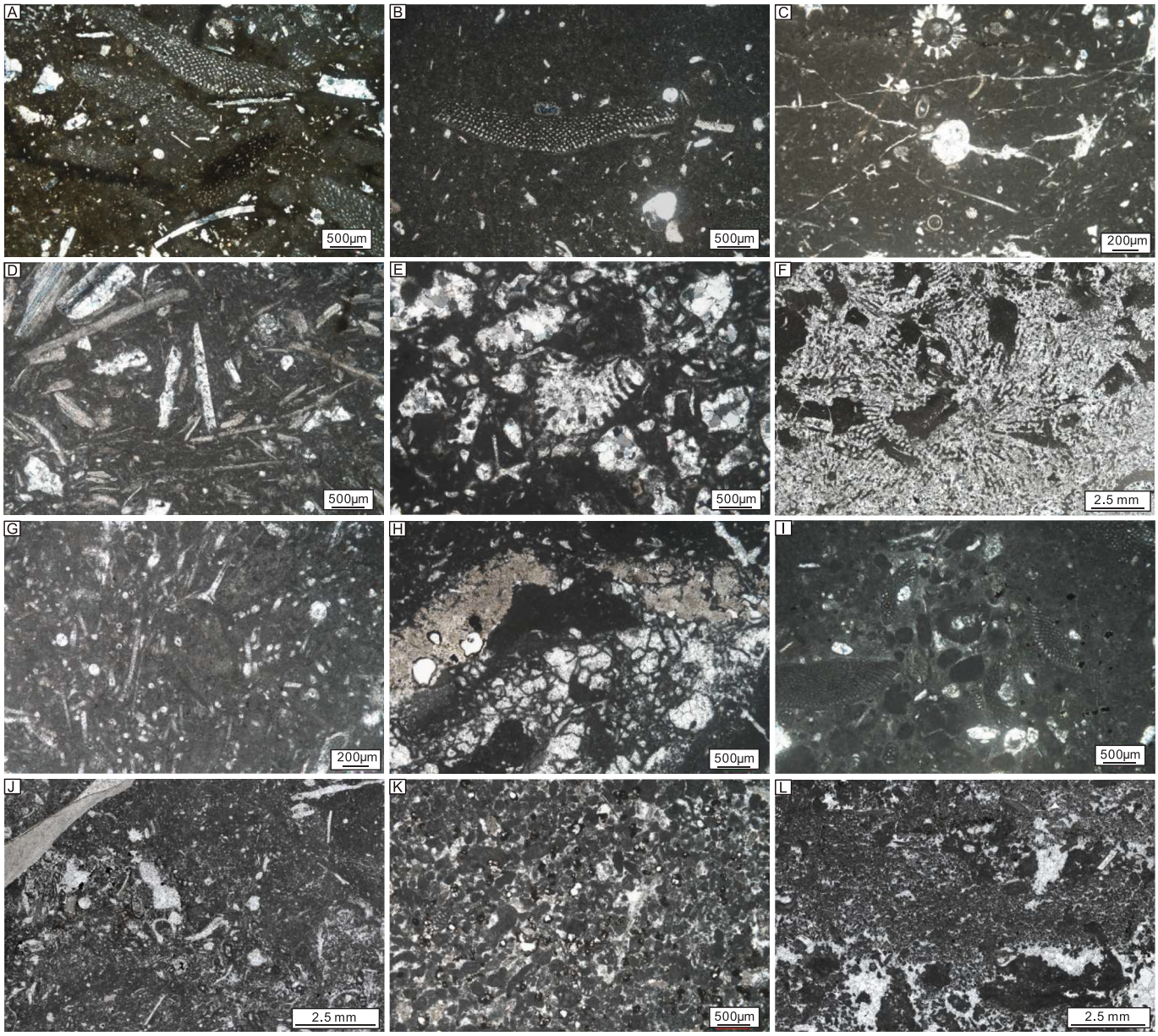


**Fig. 5.** A) Orbitolinids rudstone, 19KJ46. B) Bioclastic wackestone, 19KJ35. C) Spicule wackestone with algae, 19KJ01. D) Rudist floatstone, 19KJ02. E) Bivalve packstone, 19KJ04. F) Coral rudstone, 19KJ06. G) Spicule wackestone, 19KJ42. H) *Bacinella*-rudist wackestone, 19KJ12. I) Orbitolinids wackestone with small benthic foraminifers, 19KJ26. J) Bioclastic wackestone, 19KJ12. K) Lumps-peloids packstone, 19KJ18. L) Lumps-peloids grainstone with bird's eyes, 19KJ14.

*4.2.1.7. MF7 Sponge spicule-rudist biostrome.* Thick-bedded, intensely bioturbated limestones in both lower and upper parts of the Dariyan Formation contain densely packed in situ rudists (Fig. 2F) set in micritic matrix that contains common monaxons or triaxons spicules with central canals belonging to siliceous sponges (Fig. 5G). Small benthic foraminifers, rudist debris, *Bacinella*, green algae, and echinoderms occur. Rudists thrive in shallow shelfal environments (Ross and Skelton, 1993; Özer et al., 2017) and microfacies MF7 is overlain by MF1, suggesting a shallower water depth than MF3 at the transition from shallow to deep subtidal environments.

### 4.2.2. Shallow subtidal environment

*4.2.2.1. MF8 Bacinella-rudist wackestone.* Medium- to thick-bedded limestones widely distributed throughout the Khormoj section contain well-preserved rudists mostly encrusted by *Bacinella*, a rather enigmatic calcimicrobial structure (Fig. 5H). Small benthic foraminifers, including miliolids and textulariina, are common. Orbitolinids, crinoids, other bivalve debris, peloids, and intraclasts occur. Some bioclasts are strongly micritized. *Bacinella* typically occurs in reef crest or lagoonal environments (Stein et al., 2012; Kaya and Altıner, 2015) and the well-preserved in situ rudists indicate a biostrome in a shallow subtidal environment.

### 4.2.3. Lagoon

*4.2.3.1. MF9 Orbitolinid wackestone with small benthic foraminifers.* Thick-bedded limestones in the upper Dariyan Formation contain abundant benthic foraminifers set in micritic matrix. Unlike MF1 and MF2, other small benthic foraminifers (miliolids, textulariina, and rotaliids) are common in addition to flat orbitolinids (Fig. 5I). Echinoderms, gastropods, and spicules are rare. The co-occurrence of orbitolinids and diversified benthic foraminifers suggests a shallower environment than MF1 and MF2. The abundance of micrite indicates low-energy conditions in a shallow subtidal lagoon.

*4.2.3.2. MF10 Bioclastic wackestone with small benthic foraminifers.* Thick-bedded limestones in the upper part of the Khormoj section mainly consist of small benthic foraminifers (miliolids and textulariina; up to ~12%) (Fig. 5J) associated with echinoderms, bivalves, sponge spicules, and orbitolinids. Peloids and lumps are locally abundant. Common miliolids and textulariids indicate a shallow lagoonal environment with water depth ≤ 10 m (Ghabeishavi et al., 2010).

### 4.2.4. Intertidal to supratidal environment

*4.2.4.1. MF11 Lump wackestone with small benthic foraminifers.* Thin- to medium-bedded limestone in the middle part of the Khormoj section contain abundant lumps and peloids set in micritic matrix (Fig. 5K). Small benthic foraminifers and small bioclasts are common. Echinoderms, orbitolinids and intraclasts are rare. Abundant lumps and peloids and micritic matrix indicate a low-energy restricted lagoonal to intertidal environment (Jones, 2010).

*4.2.4.2. MF12 Lump-peloid grainstone with bird's eyes.* Thin-bedded limestones in the middle part of the Khormoj section mostly contain lumps and peloids with rare miliolids and other bioclasts. Thin laminations and bird's eyes are common (Fig. 5I), indicating an upper intertidal to supratidal environment unsuitable for the life of organisms (Flügel, 2010).

### 4.2.5. Environmental evolution

Microfacies analysis of the upper Dariyan Formation documents a regression followed by a transgression (Fig. 6). The gradual regression starts with MF3-MF6, representing a deep subtidal environment influenced by storm activity at the base of the measured Khormoj section, overlain by MF11-MF12 deposited in peritidal environments (Fig. 6). In the middle part of the section, MF8-MF10 indicate a change from peritidal to shallow subtidal environments, thus heralding a transgression (Fig. 6). Subsequently, deep subtidal deposition of MF2 followed by MF7 indicates progressive transition to deeper subtidal environments in the upper part of the section (Fig. 6). Microfacies MF1 at the top of the Dariyan Formation documents renewed transgression during which deepest-water conditions were reached (Fig. 6). Subaerial exposure of the carbonate platform is indicated by the paleosol at the top of the Dariyan Formation (Fig. 2E).

### 4.3. Carbon-isotope stratigraphy

Carbonate carbon isotopes show significant fluctuations from 1‰ to 4‰ in lower Aptian strata. Seven discrete segments (labeled from C1 to C7 in Fig. 6) are recognized following the classification of Menegatti et al., 1998). The $\delta^{13}C$ values remain stable (+2.6 to 2.9‰) in stage C2, sharply fall to +1.1‰ at the C2/C3 boundary, remain between +1.1‰ and + 1.3‰ in stage C3 (with one peak at +1.6‰.), shift from +1.3‰ to +2.0‰ in stage C4, and remain around +2.0‰ in stage C5. Then $\delta^{13}C$ values shift rapidly from +2.0‰ to +4.2‰ in stage C6, remaining between +3.0 ‰ and + 4.0‰ in stage C7, considered as a carbon-isotope plateau.

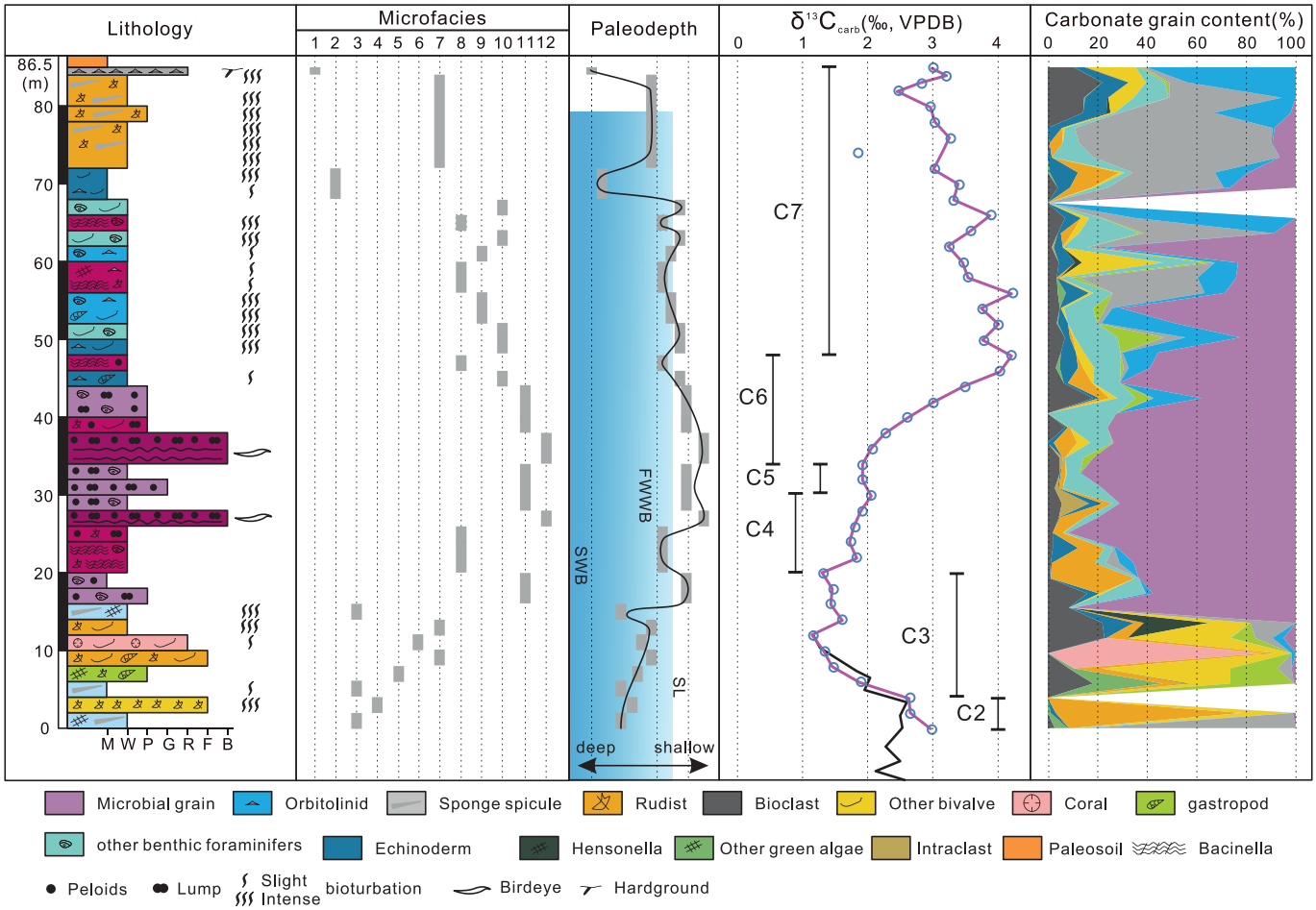


**Fig. 6.** Stratigraphic log of Dariyan Formation at Khormoj section showing identified microfacies, carbonate-grain types, reconstructed paleodepth curve, and whole-rock carbonate $\delta^{13}C$. Black line of carbon-isotope data from Vincent et al. (2010). SL, sea level; FWWB, fair weather wave base; SWB, storm wave base; TE, transgressive event; VPDB, Vienna Pee Dee Belemnite.

### 4.4. Quantitative analysis of carbonate grains

Carbonate grains include: (1) skeletal grains (macrofossil debris of rudists, corals, gastropods, benthic foraminifers, echinoderms, green algae, and undetermined bioclasts); (2) microbial grains (peloids, lumps, and *Bacinella*); and (3) intraclasts. Point-counting data showed a dominance of corals, rudists and other bivalves in C2 to early C3 stages (Fig. 6), with sharp increase of microbial grains to 57–90% in late C3 to C6 stages. Microbial grains decreased from 55% to 15% in the early C7 stage and were finally replaced by sponge spicules, rudists and orbitolinids in the C7 stage, where orbitolinids reach up to 60% (Fig. 6).

### 4.5. Major and trace element geochemistry

The concentration of aluminum and barium throughout the measured Khormoj section shows little variation (Al ~15 ppm and Ba ~1 ppm), but for a positive excursion at the top of the Dariyan Formation (Fig. 7). The P/Ca ratio in most samples ranges from 0 to 40 (average ~ 20), but for two positive excursions in the upper part of the measured section (Fig. 7). Although REEs may be contaminated by terrigenous siliciclastic detritus, the Y/Ho ratio is mostly >36 (supplementary table S2), typical of a marine signal (Nozaki et al., 1997; Ling et al., 2013). The cerium anomaly shows significant variation throughout the measured section. Ce/Ce* remains stable (~0.9) during C2-early C3 stages, falls to 0.5 in the late C3 stage, eventually increases to 1.0–1.25 in the C7 stage followed by a negative excursion at the top of the Dariyan Formation (Fig. 7). The U content follows a similar trend, decreasing from 1.6 ppm to 0.4 ppm during stages C3-C6 and increasing to 1.5 ppm at stage C7, followed by a negative excursion (Fig. 7).

## 5. Discussion

### 5.1. Assessment of diagenetic effects on carbon isotope data

Diagenetic processes, such as dissolution and recrystallization, can modify the original isotopic composition of marine carbonates (Banner and Hanson, 1990). Carbonate mudstones, wackestones, and packstones of the Dariyan Formation, however, do not show evidence of micrite recrystallization. All $\delta^{13}C$ values vary from +1‰ to +4.5‰, and $\delta^{18}O$ values from −3.5‰ to −8‰ (Fig. 8). Samples from intertidal and supratidal environments contain bivalves and pores filled with meteoric sparite, and yet the cross-plot in Fig. 8A shows no covariation between $\delta^{18}O$ and $\delta^{13}C$. The Mn/Sr ratio, used to assess post-depositional alteration in carbonates (Brand and Veizer, 1980; Kaufman and Knoll, 1995), is very low (<1) in most studied samples, and no correlation is observed between $\delta^{13}C$ and Mn/Sr (Fig. 8B).

Carbon-isotope values may also vary depending on the presence of different carbonate grains in different microfacies (Geyman and Maloof, 2021). Stages C3-C7 are dominated by microfacies MF3–8 and MF11–12, and $\delta^{13}C$ values nevertheless remain in the +1.5‰ to +3.0‰ range, suggesting that they are independent of microfacies (Fig. 8C). Although $\delta^{13}C$ values for microfacies MF9–10 tend to be higher, the early C7 stage, dominated by MF9–10, shows a negative rather than a positive shift (Fig. 8C). All lines of evidence thus indicate that carbonate $\delta^{13}C$ values reflect mainly primary signals of seawater throughout the measured section.

### 5.2. Correlation of $\delta^{13}C$ curves and identification of OAE 1a

The OAE1a event is testified by a globally synchronous positive shift in carbon isotopes preceded by a negative excursion (Jenkyns, 2010; Skelton and Gili, 2012; Hu et al., 2020), features documented by carbon-

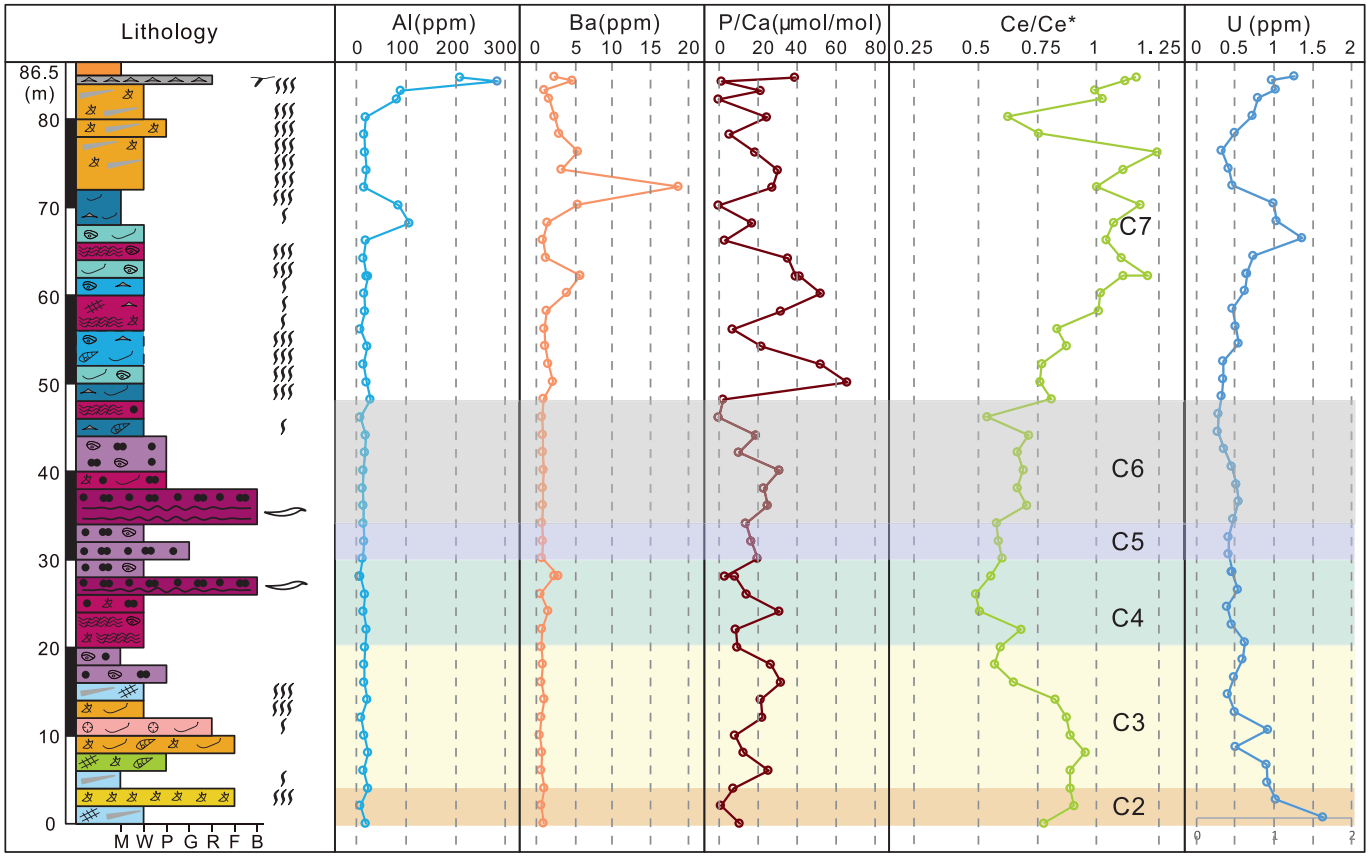


**Fig. 7.** Geochemical data from Khormoj section, including concentration of chemical elements and Ce anomaly. Legend as in Fig. 6.

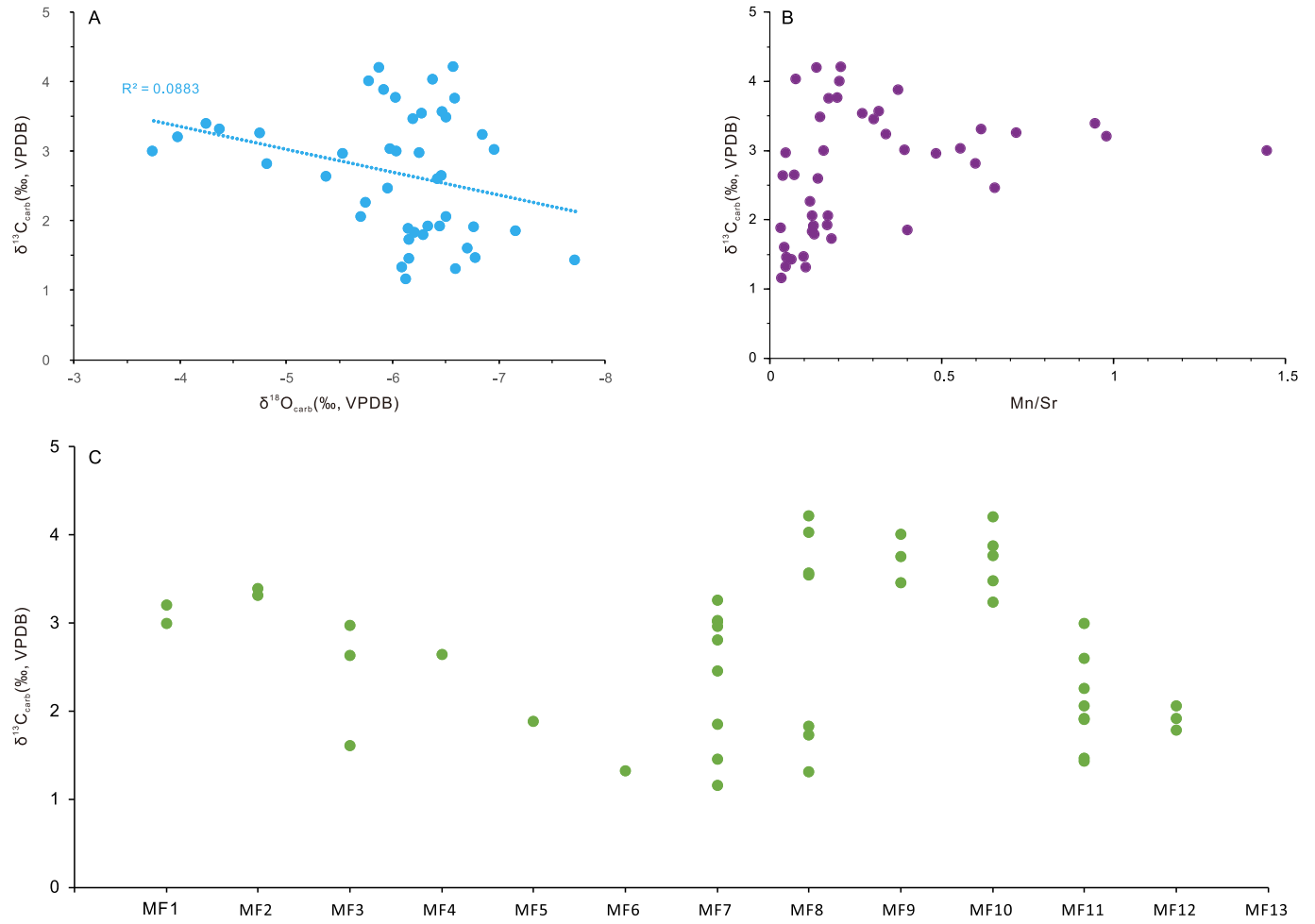


**Fig. 8.** A) Cross-plot of $\delta^{13}C$ and $\delta^{18}O$ values. B) Cross-plot of Mn/Sr and $\delta^{13}C$ values. Lack of significant covariance and low Mn/Sr indicate no significant diagenetic alteration of stable isotope values in carbonate rocks of Khormoj section. C) Range of $\delta^{13}C$ values from different microfacies of Khormoj section: no relationship is seen between $\delta^{13}C$ and microfacies.

isotope stages C3-C6 (Fig. 9). As shown by Vincent et al. (2010), carbonate $\delta^{13}C$ values decrease after stage C2 from ~3.5‰ to ~3‰, an excursion also documented in shallow-water carbonates of Pacific atolls, Italy, and Mexico (Jenkyns and Wilson, 1999; Menegatti et al., 1998; Núñez-Useche et al., 2020) (Fig. 9). The interval between 4 and 20 m from the base of the Khormoj section is assigned to stage C3, characterized by a pronounced negative $\delta^{13}C$ shift of ~2‰. This is similar to amplitudes of $\delta^{13}C$ recorded in other areas and explained by either massive release of $^{13}C$-depleted carbon related to Ontong-Java or Kerguelen large-igneous-province eruptions (Erba et al., 2015; Charbonnier and Föllmi, 2017; Jiang et al., 2022) or dissociation of methane hydrates (van Breugel et al., 2007). A positive $\delta^{13}C$ excursion from 1.3 ‰ to 2.0 ‰ characterizes stage C4, documented between 20 and 30 m above the base of the measured section. Such amplitude is similar as that recorded in Italy, but slightly lower than carbon isotope documented in Turkey and Pacific atolls (Fig. 9). The carbon-isotope plateau (stage C5), occurring between 30 and 34 m above the base of the measured section, is followed by a positive excursion of ~2–4‰ (stage C6), which defines the end of OAE1a at 48 m from the base of the studied section. Finally, decreasing $\delta^{13}C$ values in the upper 38.5 m (from 48 m to the top at 86.5 m) define stage C7. Late stage C7, characterized by $\delta^{13}C$ values of ~4‰ in other shallow and pelagic carbonate sections (Fig. 9), may not be entirely recorded in the Khormoj section because of subaerial erosion (Vincent et al., 2010).

In the Khormoj section, the OAE1a event (stages C3-C6) is represented over a stratal thickness of 40 m, comparable to shallow-water carbonates in Spain and Mexico (~30 m) but notably thinner than for Pacific atolls (~130 m) and much thicker than pelagic equivalents (~2.1 m in Turkey and ~ 6 m in Italy) (Fig. 9). The expanded record of the OAE1a event in shallow-water carbonate platforms allows a more precise assessment of sedimentary evolution and reconstruction of relative sea-level change.

### 5.3. *Sedimentary response to OAE1a: sea-level or environmental stress?*

The responses of Tethyan carbonate platforms to the OAE1a event are widely documented with two different modalities. Most carbonate platforms drowned before OAE1a along the northern margin of Neotethys, whereas they continuously accumulated along the southern margin of Neotethys even although with significant biotic changes (Huck et al., 2011, 2014; Skelton and Gili, 2012). On the southern Neotethyan and proto-North Atlantic margins, carbonate producers are mostly represented by oligotrophic assemblages (i.e., rudists and green algae), which were replaced by mesotrophic assemblages (i.e., *Lithocodium*, *Bacinella, Orbitolinids*) during OAE1a (Huck et al., 2014; Núñez-Useche et al., 2020). Such transition was ascribed to eutrophication, hypoxia, or other environmental stresses (Skelton and Gili, 2012; Huck et al., 2014; Hueter et al., 2019; Núñez-Useche et al., 2020).

A similar change in carbonate producers, with development of *Lithocodium–Bacinella* buildups during OAE1a, was reported from the Arabian margin in Oman (Immenhauser et al., 2005; Rameil et al., 2010). The same increase in *Lithocodium–Bacinella* and other microbial

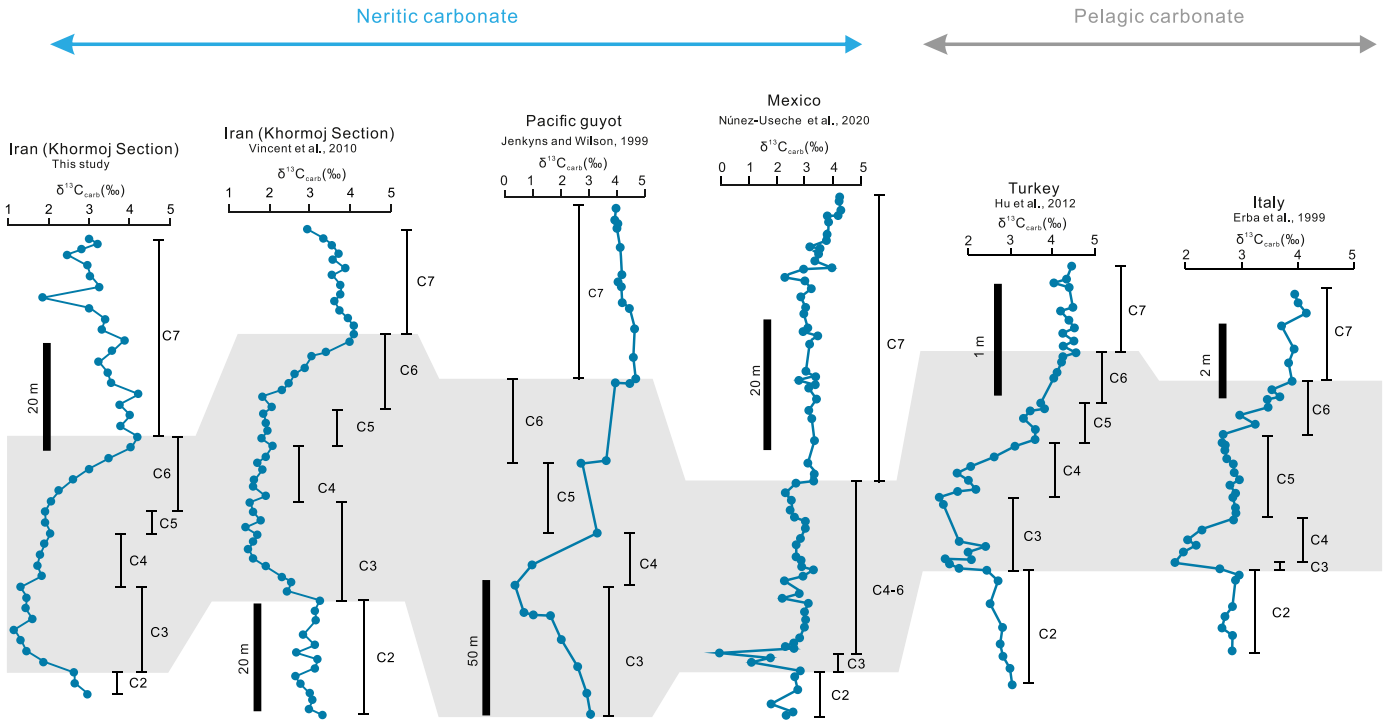


**Fig. 9.** Correlation of $\delta^{13}C$ curves from carbonates of Khormoj section (this study and Vincent et al., 2010) with other sections worldwide (Pacific atoll: Jenkyns and Wilson, 1999; Mexico: Núñez-Useche et al., 2020; Turkey: Hu et al., 2012; Italy: Menegatti et al., 1998).

grain during OAE1a was identified in the Dariyan Formation in southern Iran (Naderi-Khujin et al., 2016; Bahrehvar et al., 2020). In the measured Khormoj section, a transition of carbonate producers from rudists and other skeletal grains to *Bacinella* and other microbial nonskeletal grains with decreased bioturbation is well documented during stages C4-C6 (Fig. 6).

Although such a change may have been induced by eutrophication or hypoxia, in the studied section the sedimentary environment changed from subtidal to peri-tidal from stage C3 to C4, a regression well documented by microfacies (e.g., bird's eye structure in MF12). Biodiversity and bioturbation are expected to decrease in stressful supratidal environments, where microbial organisms, peloids, and aggregates become predominant (Flügel, 2010). The observed biotic changes may thus be ascribed to a relative change in sea level as well.

Geochemical proxies do not support eutrophication or deoxygenation during the OAE1a event in the Khormoj section. Al concentration, a proxy of terrigenous input (Tribovillard et al., 2006), is mostly very low (~8–20 ppm) and invariably <150 ppm, implying no siliciclastic pollution. P and Ba concentrations, widely used as proxies of productivity (Tribovillard et al., 2006; Schoepfer et al., 2015), show little variation during stages C2-C6, implying no drastic changes in productivity or eutrophication caused by accelerated continental weathering (Fig. 7).

The Ce/Ce* value, a valuable proxy of redox conditions (Tribovillard et al., 2006; Ling et al., 2013), shows a gradual negative shift from 0.8 to 0.5 between the late C3 and C4 stages, indicating a more oxic state as the depositional environment changed from subtidal to peritidal (Fig. 7). At stages C5-C7during transgression, Ce/Ce* increased to ~1.25 indicating a decrease in seawater oxygenation. The concentration of U, which increases in anoxic environments and can thus be used as a redox proxy (Tribovillard et al., 2006), decreased from 1.6 ppm to 0.4 ppm during stages C3-C6, and then increased to 1.5 ppm at stage C7 (Fig. 7). Both Ce anomaly and U concentration thus reflect oxygenic rather than anoxic conditions during OAE1a in the Khormoj section, which rules out the hypothesis that the observed change in carbonate was producers caused by eutrophication and hypoxia.

The observed coherent trends in the Ce anomaly and U concentration are instead consistent with changes in relative sea level, both increasing during transgression and decreasing during regression. For instance, the drastic increase in Ce/Ce* and U concentration at the top of the measured section corresponds to a change from microfacies MF7 to MF1–2 related to transgression. We thus conclude that relative changes in sea level represent a more plausible control on the biotic changes observed during the OAE1a event than changes in seawater chemistry.

### 5.4. *Eustatic changes during OAE1a*

Positive shifts in carbon isotopes and accumulation of sediments enriched in organic carbon during the OAE1a event have been widely associated with sea-level rise and platform drowning (Föllmi et al., 1994; Grötsch et al., 1998; Millán et al., 2009; Huck et al., 2011). However, such a correlation may be partly spurious because of two main factors: 1) condensed sedimentation in deep-water settings, where strata deposited during OAE1a are six times thinner than in shallow-water settings (Fig. 9); 2) redox state of deep seawater, which may change from oxic to anoxic conditions (Jenkyns, 2010; Westermann et al., 2013) thus favoring the accumulation of organic-carbon-rich sediments independently of sea-level change. Moreover, carbonate-platform drowning along the northern margin of Neotethys took place before the onset of stage C3 (Huck et al., 2011; Najarro et al., 2011; Masse and Fenerci-Masse, 2013; Frau et al., 2020), which indicates that drowning may not have been caused by either eustatic rise or the OAE1a event.

Thicker shallow-water carbonates provide a more comprehensive record of high-frequency relative sea-level changes. In the measured Khormoj section, strata deposited during stage C2 are dominated by orbitolinids and other open marine faunas, and the maximum flooding surface corresponds to the top of stage C2 (Vincent et al., 2010). Strata deposited during stage C3 are instead dominated by rudists, indicating reduced paleodepth, a regressive trend that culminates with peritidal deposition during stage C4. The transgressive trend is resumed during stage C6, with shallow subtidal deposition passing upward to deep subtidal conditions in stage C7 (Fig. 10).

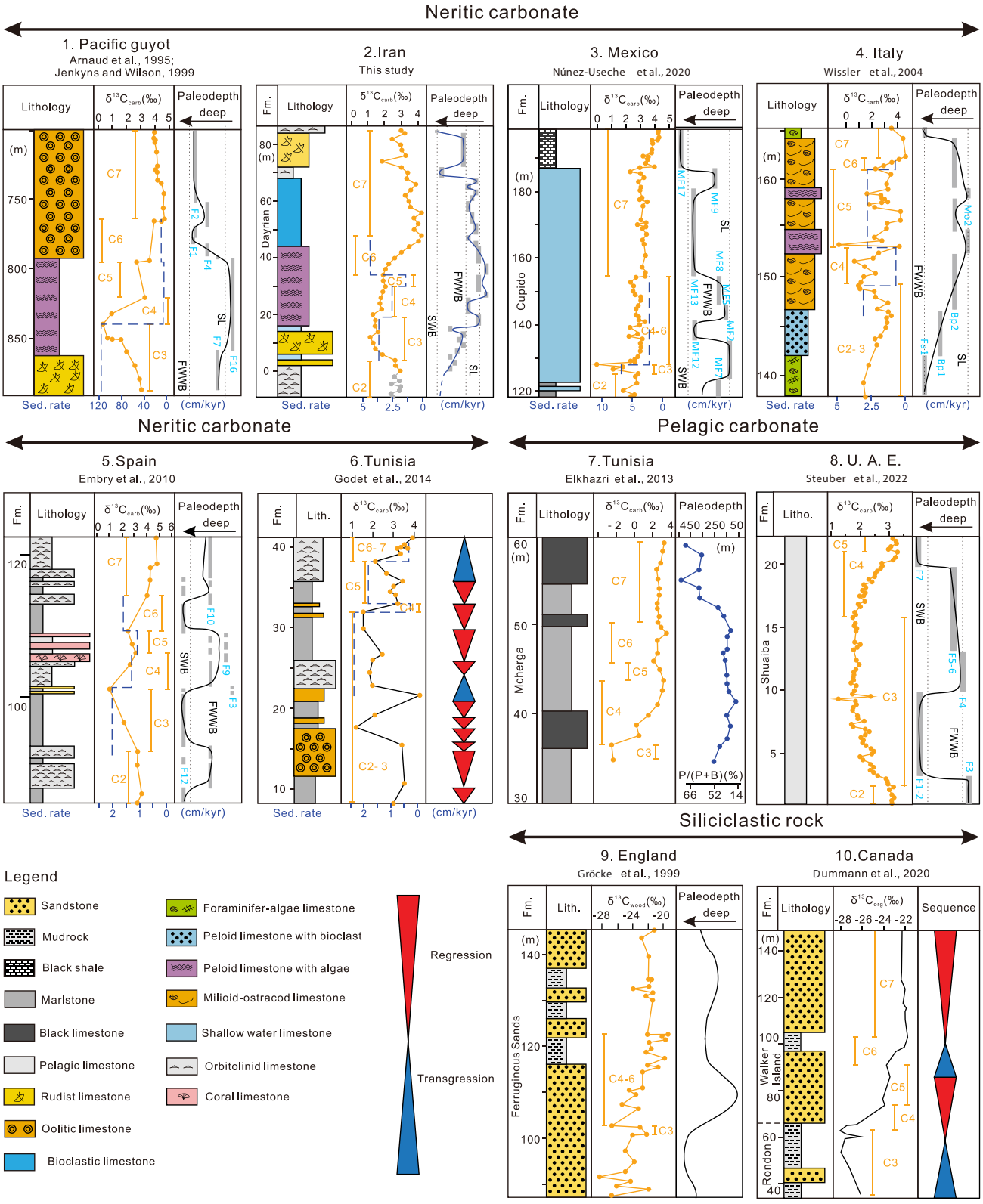


**Fig. 10.** Correlation of paleowater-depth changes and depositional sequences during OAE1a in ten stratigraphic sections worldwide. Six neritic sections are from Pacific guyot (Jenkyns and Wilson, 1999), Iran (this study), Mexico (Núñez-Useche et al., 2020), Italy (Wissler et al., 2004), Spain (Embry et al., 2010) and Tunisia (Godet et al., 2014); two pelagic sections are from Tunisia (Elkhazri et al., 2013) and the United Arab Emirates (Steuber et al., 2022), and two siliciclastic sections from England (Gröcke et al., 1999) and Canada (Dummann et al., 2021). For each section (location shown in Fig. 1), lithology, carbon isotopes, paleodepth/depositional sequences, and sedimentation rate (for stages C3-C6 only for six neritic sections #1–6) are indicated. The $\delta^{13}C$ data from the base of the Khormoj section (gray points) and the dashed paleodepth curve are from Vincent et al. (2010). The blue dashed line shows changes in sedimentation rate during stages C3-C6 (duration of each stage after Beil et al., 2020). In light blue are facies codes defined in each of the cited references. Depositional environments and corresponding water depths are provided in supplementary table S3. (For interpretation of the references to colour in this figure legend, the reader is referred to the web version of this article.)

Pacific guyots record a similar regressive-transgressive trend (Arnaud et al., 1995; Jenkyns and Wilson, 1999). Shallow subtidal rudist grainstone passes upward to peritidal mudstone at stages C3-C5, followed by deposition of oolites in an open marine environment at stages C6-C7 (Fig. 10).

On the Cupido platform in the Gulf of Mexico, laminated wackestone deposited on an inner ramp during stage C2 pass upward to peritidal microbial bindstone in stage C3 recording the onset of the positive $\delta^{13}C$ shift (Núñez-Useche et al., 2020). An abrupt transgression documented by deposition of echinoderm grainstone on a middle ramp occurred at stages C4-C6, culminating in platform drowning and deposition of mudstone with planktonic foraminifers at stage C7 (Fig. 10).

In Italy (Wissler et al., 2004), a regression documented by transition from open-marine foraminiferal-algal limestone to inner shoal biopeloidal limestone occurred at stages C2-C3, continuing with deposition in a restricted lagoon at stage C4. Strata accumulated in restricted-lagoon and peritidal settings alternate at stages C5-C6, followed by a major transgression testified by deposition of open-marine limestone at stage C7 (Fig. 10).

In NE Spain, offshore marls replaced upwards by coral boundstone indicates a regression during stages C3-C5, followed by transgression at stage C6 (Embry et al., 2010, Fig. 10). Moreover, shallow-water carbonates in Tunisia also document a shallowing-upward sequence at stages C3-C5 and a deepening-upward sequence at stages C6-C7 (Godet et al., 2014, Fig. 10). All shallow-water carbonates mentioned above thus recorded regression from subtidal to peritidal environments at stages C3-C4, followed by transgression at stage C6 and maximum flooding in the early C7 stage.

The regression at stages C3-C4, however, may have been caused by different factors, including tectonic uplift, increased carbonate production, or sea-level fall. Tectonic uplift would imply strong reduction of accommodation space and formation of an unconformity, whereas increased carbonate productivity would imply an increased accumulation rate. Shallow-water carbonates deposited during stages C3 and C4, instead, show a decrease in accumulation rate that is best explained by sea-level change (section 1–6 of Fig. 10).

Similar paleowater-depth trends are recorded in some pelagic carbonate and siliciclastic successions (Fig. 10). In organic-rich, black pelagic limestones of Tunisia, the ratio between planktonic and benthic foraminifers decreases from 52 to 22% during stage C4, indicating decreasing paleowater depth (Elkhazri et al., 2013). Paleodepth remained relatively constant during stage C5 and clearly increased at stage C6, reaching maximum at stage C7 (Elkhazri et al., 2013). In the Bad Basin of the United Arab Emirates, a regression documented at stage C3 is followed by transgression in the late C4-C5 stages (Steuber et al., 2022) (Fig. 10). In siliciclastic successions in England, an up-section increase in the sandstone/shale ratio from offshore to nearshore settings is documented during the positive $\delta^{13}C$ excursion (Gröcke et al., 1999) (Fig. 10). In arctic Canada, a similar regression is testified by the transition from offshore siltstone to shoreface sandstone during stage C4 (Dummann et al., 2021, Fig. 10).

The ten different stratigraphic sections discussed above thus display

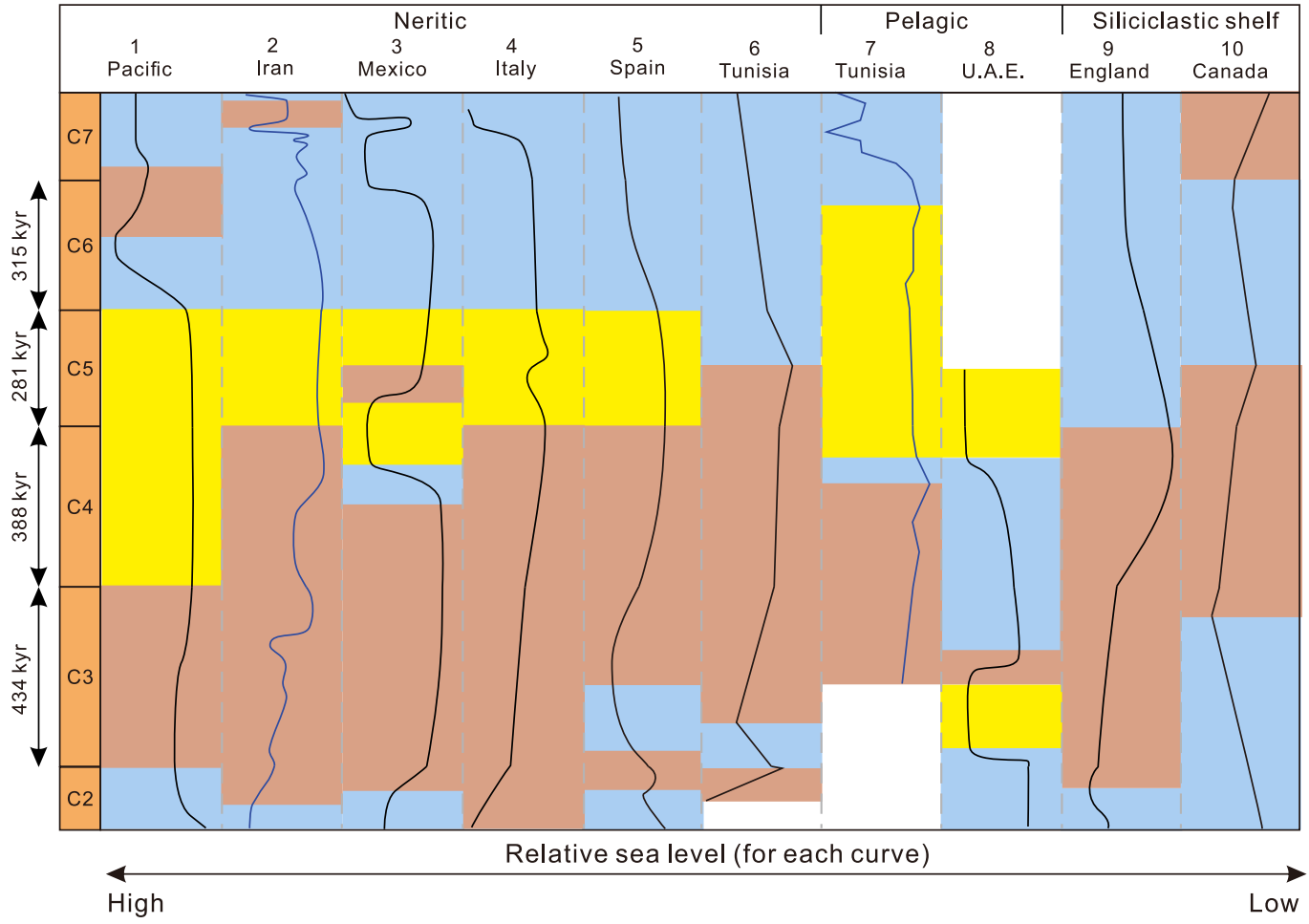


**Fig. 11.** Comparison of relative sea-level changes documented during the OAE1a interval in ten selected sections worldwide. Transgressive, stillstand, and regressive stages are outlined in blue yellow, and brown, respectively. (For interpretation of the references to colour in this figure legend, the reader is referred to the web version of this article.)

a similar major regressive-transgressive trend during OAE1a, which can be explained as eustatically controlled. The regression generally started at stage C3, continued at stage C4, was followed by relative constant sea level during stage C5 and finally by gradual transgression during stage C6, eventually leading to maximum flooding in the early C7 stage (Fig. 11). Eustatic rise resulting in expansion and impingement onto the shelf of the oxygen minimum zone has been widely invoked as a direct contributing mechanism of black-shale deposition during OAEs (Föllmi et al., 1994; Grötsch et al., 1998; Bond and Wignall, 2008; Hermoso et al., 2013; Bartlett et al., 2018; Reershemius and Planavsky, 2021). During stage C4, the positive $\delta^{13}C$ shift was widely associated with black-shale deposition and enrichment of total organic carbon (Menegatti et al., 1998; Jenkyns, 2010; Erba et al., 2015; Castro et al., 2021). We note, however, that in the studied localities relative sea-level was falling rather than rising during stage C4, implying that eustatic rise was not the cause of black-shale accumulation. Instead, eustatic fall may have led to weathering on the newly exposed land surfaces, with consequent decreased $CO_2$ concentration and global temperature, and increased nutrient input to the ocean. Increased primary productivity may have thus represented the main cause of increased organic carbon burial and of the positive $\delta^{13}C$ excursion during OAE1a.

### 5.5. Drivers of eustatic change and climate evolution

Short-term eustatic changes consequent to changes in sea-water volume have three main known mechanisms, thermo-eustasy, aquifer-eustasy, and glacio-eustasy, the latter being able to induce effects of notably larger amplitude (Ray et al., 2019; Davies et al., 2020). Thermo-eustasy is driven by temperature changes in seawater which lead to thermal (volume) expansion or contraction, whereas glacio-eustasy or aquifer-eustasy are caused by waxing and waning of continental ice sheets or charging and discharging of continental aquifers (Sames et al., 2020). During global warming, both thermo-eustasy and glacio-eustasy lead to eustatic rise, whereas eustatic fall may result from enhanced water transfer from the ocean to continental aquifers (Wendler and Wendler, 2016; Li et al., 2018; Sames et al., 2020). Stage C3 is widely considered as documenting rapid warming caused by the abundant release of carbon dioxide from the Ontong Java or Kerguelen large igneous provinces (Fig. 12; Charbonnier and Föllmi, 2017; Erba et al., 2015; Jiang et al., 2022). The stratigraphic sections discussed above (Fig. 11), instead, record a regressive trend at this stage, which we here suggest to have been mainly controlled by aquifer-eustasy. The amplitude of paleowater-depth changes decreased from stage C2 (10–20 m) to C3 (5–10 m) and relative sea-level remained almost stationary during stage C5 (Fig. 12), which is compatible with the estimated magnitude of aquifer eustasy (Davies et al., 2020). The transgression recorded during the C6 to early C7 stages, when accelerated burial of organic carbon induced climatic cooling (Jenkyns, 2010, 2018), still indicates aquifer-eustasy. Based on age models estimated from cyclostratigraphy – which however vary among pelagic sections, especially for the C3 stage poorly constrained from 41 and 485 kyr (Li et al., 2008; Hu et al., 2012; Beil et al., 2020; Charbonnier et al., 2023), the duration of eustatic changes of C3-C6 stages is about 1.0 to 1.4 myr (Supplementary table S5). Correspondence with ~1.2 myr obliquity cycles thus led to speculate the orbital forcing may contribute to eustatic change via aquifer eustasy (Boulila et al., 2011, 2021).

## 6. Conclusion

This study integrates new and published sedimentological, biostratigraphic, and geochemical data on shallow-marine carbonates exposed in the Zagros orogen (Khormoj section of the Dariyan Formation, southern Iran) to reconstruct the sedimentary evolution during the early Aptian OAE1a. Biostratigraphic and carbonate carbon isotopes here precisely identify the OAE1a within a 40-m-thick interval. Carbonate grains were dominantly corals, rudists and other bivalves in C2 to early C3 stages, and microbial grains in the late C3-C6 stages. Microbial grains sharply decreased in the early C7 stage and were replaced by sponge spicules, rudists and orbitolinids in the late C7 stage. Microfacies analysis testifies to a regression from thick-bedded deep-subtidal carbonates to thin-bedded peritidal carbonates during stages C3-C4, followed by slow transgression with return to shallow subtidal deposition during stage C6. The transgressive trend continued during the early C7 stage, when maximum paleodepth was reached. Geochemical proxies indicate low-nutrient and oxygen-rich conditions during OAE1a, suggesting sea-level control rather than changing seawater chemistry. Correlation with relative sea-level changes documented in other Tethyan, northern Atlantic, Pacific, and Arctic areas consistently indicate that a regression at stages C3-C4 was followed by a transgression at stages C6-C7, pointing at eustatic control. Regression occurred at during warming and transgression during cooling, and maximum magnitude of eustasy decreased down to 5–10 m during stages C4-C6. All pieces of evidence combined indicate that aquifer-eustasy, rather than thermo-eustasy or glacio-eustasy, most plausibly represented the main cause of eustatic change during OAE1a.

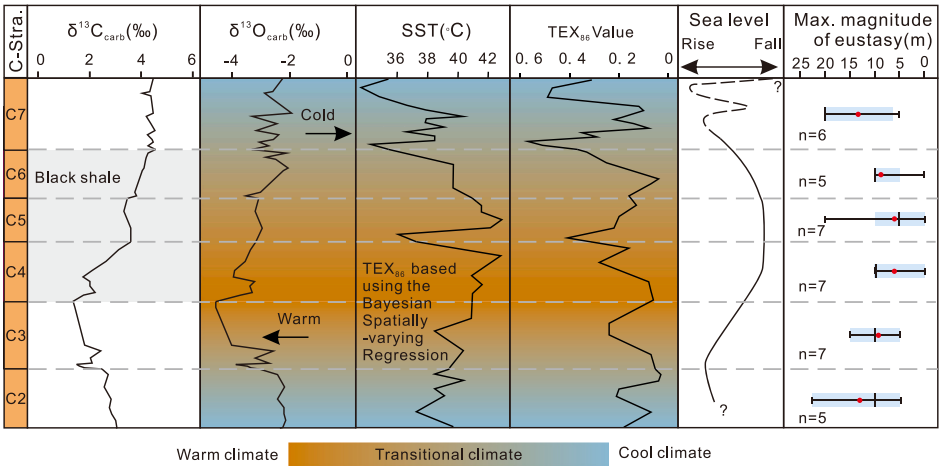


**Fig. 12.** Inferred eustatic changes duing OAE1a and correlation with $\delta^{13}C$ (Hu et al., 2012), $\delta^{18}O$ (Hu et al., 2012), and sea surface temperature (SST), and $TEX_{86}$ (Naafs and Pancost, 2016) curves. Estimation of maximum magnitude of eustatic fluctuations (notably larger for the Tunisia sectionnot included here) are based on facies change and are considered to be conservative (supporting dataset provided in supplementary table S4).

## Declaration of Competing Interest

The authors declare that they have no known competing financial interests or personal relationships that could have appeared to influence the work reported in this paper.

## Data availability

No data was used for the research described in the article.

## Acknowledgments

This paper is dedicated to Li Juan, who left us while logging the PETM interval in Tibet. Yiwei Xu's study on microfacies analysis could not have been improved without her assistance and guidance. We thank Jitao Chen, Zhong Han, Yutian Zhong, Hao Xin and Yinggang Zhang for discussion, Haiyan Shen, Miao Lv, and Guang Li for assistance in the laboratory. We also thank editor Alan Haywood and two anonymous reviewers for their thoughtful feedback that helped improve this manuscript. This study was financially supported by the National Natural Science Foundation of China (41888101, 42072124, 42072117, 42202118), Open Research Fund of State Key Laboratory of Mineral Deposit Research at Nanjing University (2023-LAMD-K10) and Jiangsu Funding Program for Excellent Postdoctoral Talent. This study is a contribution to the IGCP 739.

## Appendix A. Supplementary data

Supplementary data to this article can be found online at https://doi.org/10.1016/j.gloplacha.2023.104236.

## References

Afghah, M., Haghighi, A.S., 2014. Aptian biostratigraphy in South Zagros Basin, Southwest Iran. Geosci. Front. 5 (2), 277–288.
Alley, N.F., Hore, S.B., Frakes, L.A., 2019. Glaciations at high-latitude Southern Australia during the Early Cretaceous. Aust. J. Earth Sci. 1–51.
Arnaud, H.M., Flood, P.G., Strasser, A., 1995. Resolution Guyot (Hole 866A, Mid-Pacific Mountains): Facies evolution and sequence stratigraphy. In: Winterer, E.L., Sager, W. W., Firth, J.V., Sinton, J.M. (Eds.), Proc. Ocean Drill. Program Sci. Results, 143. College Station, Texas, pp. 133–159.
Bahrehvar, M., Mehrabi, H., Rahimpour-Bonab, H., 2020. Coated grain petrography and geochemistry as palaeoenvironmental proxies for the Aptian strata of the southern Neo-Tethys Ocean, Persian Gulf, Iran. Facies 66, 3.
Banner, J.L., Hanson, G.N., 1990. Calculation of simultaneous isotopic and trace element variations during water-rock interaction with applications to carbonate diagenesis. Geochim. Cosmochim. Acta 54, 3123–3137.
Bartlett, R., Elrick, M., Wheeley, J.R., Polyak, V., Desrochers, A., Asmerom, Y., 2018. Abrupt global-ocean anoxia during the late Ordovician–early Silurian detected using uranium isotopes of marine carbonates. Proc. Natl. Acad. Sci. 115, 5896–5901.
Beil, S., Kuhnt, W., Holbourn, A., Scholz, F., Oxmann, J., Wallmann, K., Lorenzen, J., Aquit, M., Chellai, E.-H., et al., 2020. Cretaceous oceanic anoxic events prolonged by phosporous cycle feedbacks. Clim. Past 16, 757–782.
Bodin, S., Godet, A., Westermann, S., Föllmi, K.B., 2013. Secular change in northwestern Tethyan water-mass oxygenation during the late Hauterivian–early Aptian. Earth Planet. Sci. Lett. 374, 121–131.
Bond, D.P., Wignall, P.B., 2008. The role of sea-level change and marine anoxia in the Frasnian–Famennian (Late Devonian) mass extinction. Palaeogeogr. Palaeoclimatol. Palaeoecol. 263 (3), 107–118.
Bottini, C., Cohen, A.S., Erba, E., Jenkyns, H.C., Coe, A.L., 2012. Osmium-isotope evidence for volcanism, weathering and ocean mixing during the early Aptian OAE1a. Geology 40, 583–586.
Boulila, S., Galbrun, B., Miller, K.G., Pekar, S.F., Browning, J.V., Laskar, J., Wright, J.D., 2011. On the origin of Cenozoic and Mesozoic "third-order" eustatic sequences. Earth Sci. Rev. 109, 94–112.
Boulila, S., Haq, B.U., Hara, N., Müller, R.D., Galbrun, B., Charbonnier, G., 2021. Potential encoding of coupling between Milankovitch forcing and Earth's interior processes in the Phanerozoic eustatic sea-level record. Earth Sci. Rev. 220, 103727.
Brand, U., Veizer, J., 1980. Chemical diagenesis of a multicomponent carbonate system–1: Trace elements. J. Sediment. Res. 50 (4), 1219–1236.
Brett, C.E., Hendy, A.J.W., Bartholomew, A.J., Bonelli Jr., J.R., McLaughlin, P.I., 2007. Response of shallow marine biotas to sea-level fluctuations: a review of faunal replacement and the process of habitat tracking. Palaios 22, 228–244.
Castro, J.M., Ruiz-Ortiz, P.A., de Gea, G.A., Aguado, R., Jarvis, I., Weissert, H., Molina, J. M., Nieto, L.M., Pancost, R.D., Quijano, M.L., Reolid, M., Skelton, P.W., Lopez-Rodríguez, C., Martínez-Rodríguez, R., 2021. High-resolution C-isotope, TOC and biostratigraphic records of OAE 1a (Aptian) from an expanded hemipelagic cored succession, western Tethys: a new stratigraphic reference for global correlation and paleoenvironmental reconstruction. Paleoceanogr. Paleoclimatol. 36 e2020PA004004.
Charbonnier, G., Föllmi, K.B., 2017. Mercury enrichments in lower Aptian sediments support the link between Ontong Java large igneous province activity and oceanic anoxic episode 1a. Geology 45 (1), 63–66.
Charbonnier, G., Boulila, S., Spangenberg, J.E., Vermeulen, J., Galbrun, B., 2023. Astrochronology of the Aptian stage and evidence for the chaotic motion of Mercury. Earth Planet. Sci. Lett. 610, 118104.
Davies, A., Gréselle, B., Hunter, S.J., Baines, G., Robson, C., Haywood, A.M., Ray, D.C., Simmons, M.D., van Buchem, F.S.P., 2020. Assessing the impact of aquifereustasy on short-term cretaceous sea-level. Cretac. Res. 104445.
Dummann, W., Schroder-Adams, C., Hofmann, P., Rethemeyer, J., Herrle, J.O., 2021. Carbon isotope and sequence stratigraphy of the upper Isachsen Formation on Axel Heiberg Island (Nunavut, Canada): high Arctic expression of oceanic anoxic event 1a in a deltaic environment. Geosphere 17, 501–519.
Dunham, R.J., 1962. Classification of carbonate rocks according to deposition texture. In: Ham, W.E. (Ed.), Classification of Carbonate Rocks, vol. 1. American Association of Petroleum Geologists, pp. 108–121.
Elkhazri, A., Abdallah, H., Razgallah, S., Moullade, M., Kuhnt, W., 2013. Carbon-isotope and microfaunal stratigraphy bounding the Lower Aptian Oceanic Anoxic Event 1a in northeastern Tunisia. Cretac. Res. 39, 133–148.
Embry, A.F., Klovan, J.E., 1971. A late Devonian reef tract on northeastern Banks Island. NWT. Bull. Can. Petrol. Geol. 19, 730–781.
Embry, J.-C., Vennin, E., van Buchem, F.S.P., Schroeder, R., Pierre, C., Aurell, M., 2010. Sequence stratigraphy and carbon isotope stratigraphy of an Aptian mixed carbonate-siliciclastic platform to basin transition (Galve sub-basin, NE Spain). Geol. Soc. Lond., Spec. Publ. 329, 113–143.
Erba, E., Bottini, C., Weissert, H.J., Keller, C.E., 2010. Calcareous nannoplankton response to surface-water acidification around oceanic anoxic event 1a. Science 329, 428e432.
Erba, E., Duncan, R.A., Bottini, C., Tiraboschi, D., Weissert, H., Jenkyns, H.C., Malinverno, A., 2015. Environmental consequences of Ontong Java Plateau and Kerguelen Plateau volcanism. In: Neal, C.R., Sager, W.W., Sano, T., Erba, E. (Eds.), The Origin, Evolution, and Environmental Impact of Oceanic Large Igneous Provinces: Geological Society of America Special Paper, vol. 511, pp. 271–303.
Fernández-Mendiola, P.A., Mendicoa, J., Hernandez, S., Owen, H.G., García-Mondéjar, J., 2013. A facies model for an Early Aptian carbonate platform (Zamaia, Spain). Facies 59, 529–558.
Flügel, E., 2010. Microfacies of Carbonate Rocks. In: Analysis, Interpretation and Application, 2nd ed. Springer-Verlag, Berlin, p. 924.
Föllmi, K.B., Weissert, H., Bisping, M., Funk, H., 1994. Phosphogenesis, carbon-isotope stratigraphy,a nd carbonate-platform evolution along the Lower Cretaceous northern Tethyan margin. Geol. Soc. Am. Bull. 106, 729–746.
Fox-Kemper, B., et al., 2021. Ocean, cryosphere and sea level change. In: Climate Change 2021: The Physical Science Basis. Contribution of Working Group I to the Sixth Assessment Report of the Intergovernmental Panel on Climate. Change Cambridge University Press.
Frau, C., Tendil, A.J.B., Pohl, A., Lanteaume, C., 2020. Revising the timing and causes of the Urgonian rudistid-platform demise in the Mediterranean Tethys. Glob. Planet. Chang. 187, 103124.
Geyman, E.C., Maloof, A.C., 2021. Facies control on carbonate $\delta^{13}C$ on the Great Bahama Bank. Geology 49 (9), 1049–1054.
Ghabeishavi, A., Vaziri-Moghaddam, H., Taheri, A., Taati, F., 2010. Microfacies and depositional environment of the Cenomanian of the Bangestan anticline, SW Iran. J. Asian Earth Sci. 37, 275–285.
Gili, E., Masse, J., Skelton, P.W., 1995. Rudists as gregarious sediment-dwellers, not reef-builders, on Cretaceous carbonate platforms. Palaeogeogr. Palaeoclimatol. Palaeoecol. 118, 245–267.
Godet, A., Hfaiedh, R., Arnaud-Vanneau, A., Zghal, I., Arnaud, H., Ouali, J., 2014. Aptian palaeoclimates and identification of an OAE1a equivalent in shallow marine environments of the southern Tethyan margin: evidence from SouthernTunisia (Bir Oum Ali section, Northern Chott Chain). Cretac. Res. 48, 110e129.
Gröcke, D.R., Hesselbo, S.P., Jenkyns, H.C., 1999. Carbon-isotope composition of Lower Cretaceous fossil wood: ocean-atmosphere chemistry and relation to sea-level change. Geology 27 (2), 155–158.
Grötsch, J., Billing, I., Vahrenkamp, V., 1998. Carbon-isotope stratigraphy in shallow-water carbonates: implications for Cretaceous black-shale deposition. Sedimentology 45, 623–634.
Hermoso, M., Minoletti, F., Pellenard, P., 2013. Black shale deposition during Toarcian super-greenhouse driven by sea-level. Clim. Past 9 (6), 2703–2712.
Herrle, J.O., Schröder-Adams, C.J., Davis, W., Pugh, A.T., Galloway, J.M., Fath, J., 2015. Mid-Cretaceous High Arctic stratigraphy, climate, and oceanic anoxic events. Geology 43 (5), 403–406.
Homke, S., Verges, J., Serra-Kiel, J., Bernaola, G., Sharp, I., Garces, M., Goodarzi, M.H., 2009. Late Cretaceous- -Paleocene formation of the proto- Zagros foreland basin, Lurestan Province, SW Iran. Geol. Soc. Am. Bull. 121 (7–8), 963–978.
Hu, X.M., Zhao, K.D., Yilmaz, I.O., Li, Y.X., 2012. Stratigraphic transition and palaeoenvironmental changes from the Aptian oceanic anoxic event 1a (OAE1a) to the oceanic red bed 1 (ORB1) in the Yenicesihlar section, Central Turkey. Cretac. Res. 38, 40–51.
Hu, X.M., Li, J., Han, Z., Li, Y.X., 2020. Two types of hyperthermal events in the Mesozoic-Cenozoic: environmental impacts, biotic effects, and driving mechanisms. Sci. China-Earth Sci. 63, 1041–1058.

Huck, S., Heimhofer, U., Rameil, N., Bodin, S., Immenhauser, A., 2011. Strontium and carbon-isotope chronostratigraphy of Barremian–Aptian shoal-water carbonates: Northern Tethyan platform drowning predates OAE 1a. Earth Planet. Sci. Lett. 304 (3–4), 547–558.
Huck, S., Stein, M., Immenhauser, A., Skelton, P.W., Christ, N., Föllmi, K.B., Heimhofer, U., 2014. Response of proto-North Atlantic carbonate-platform ecosystems to OAE1a-related stressors. Sediment. Geol. 313, 15–31.
Hueter, A., Huck, S., Bodin, S., Heimhofer, U., Weyer, S., Jochum, K.P., Immenhauser, A., 2019. Central Tethyan platform-top hypoxia during Oceanic Anoxic Event 1a. Clim. Past 15 (4), 1327–1344.
Immenhauser, A., Hillgärtner, H., van Bentum, E., 2005. Microbial foraminiferal episodes in the Early Aptian of the southern Tethyan margin, ecological significance and possible relation to oceanic anoxic event 1a. Sedimentology 52, 77–99.
Jenkyns, H.C., 2010. Geochemistry of oceanic anoxic events. Geochem. Geophys. Geosyst. 11 (3), 1–30.
Jenkyns, H.C., 2018. Transient cooling episodes during Cretaceous Oceanic Anoxic Events with special reference to OAE 1a (Early Aptian). Philos. Trans. R. Soc. A-Math. Phys. Eng. Sci. 376 (2130), 20170073.
Jenkyns, H.C., Wilson, P.A., 1999. Stratigraphy, paleoceanography, and evolution of Cretaceous Pacific guyots; relics from a greenhouse Earth. Am. J. Sci. 299 (5), 341–392.
Jiang, Q., Jourdan, F., Olierook, H.K., Merle, R.E., Bourdet, J., Fougerouse, D., Godel, B., Walker, A.T., 2022. Volume and rate of volcanic CO2 emissions governed the severity of past environmental crisis. Proc. Natl. Acad. Sci. 119, 1–10.
Jones, B., 2010. Warm-water neritc carbonates. In: James, N.P., Dalrymple, R.W. (Eds.), Facies models 4. Geological Association of Canada Geotext, vol. 6, pp. 341–369.
Kaufman, A.J., Knoll, A.H., 1995. Neoproterozoic variations in the C-isotopic composition of seawater: stratigraphic and biogeochemical implications. Precambrian Res. 73, 27–49.
Kaya, M.Y., Altıner, D., 2015. Microencrusters from the Upper Jurassic–Lower Cretaceous İnaltı Formation (Central Pontides, Turkey): remarks on the development of reefal/peri-reefal facies. Facies 61 (4), 18.
Lawrence, M.G., Greig, A., Collerson, K.D., Kamber, B.S., 2006. Rare earth element and yttrium variability in South East Queensland waterways. Aquat. Geochem. 12, 39–72.
Lechler, M., von Strandmann, P.A.P., Jenkyns, H.C., Prosser, G., Parente, M., 2015. Lithium-isotope evidence for enhanced silicate weathering during OAE 1a (Early Aptian Selli event). Earth Planet. Sci. Lett. 432, 210–222.
Li, Y.X., Bralower, T.J., Montañez, I.P., Osleger, D.A., Arthur, M.A., Bice, D.M., Herbert, T.D., Erba, E., Premoli Silva, I., 2008. Toward an orbital chronology for the early Aptian Oceanic Anoxic Event (OAE1a, 120 Ma). Earth Planet. Sci. Lett. 271, 88–100.
Li, M.S., Hinnov, L.A., Huang, C.J., Ogg, J.G., 2018. Sedimentary noise and sea levels linked to land-ocean water exchange and obliquity forcing. Nat. Commun. 9, 1004.
Ling, H.F., Chen, X., Li, D.A., Wang, D., Shields-Zhou, G.A., Zhu, M., 2013. Cerium anomaly variations in Ediacaran–earliest Cambrian carbonates from the Yangtze Gorges area, South China: implications for oxygenation of coeval shallow seawater. Precambrian Res. 225, 110–127.
Ludt, W.B., Rocha, L.A., 2015. Shifting seas: the impacts of Pleistocene Sea-level fluctuations on the evolution of tropical marine taxa. J. Biogeogr. 42, 25e38.
MacEachern, J.A., Pemberton, S.G., Gingras, M.G., Bann, K.L., Dafoe, L.T., 2007. Uses of trace fossils in genetic stratigraphy. In: Miller III, W. (Ed.), Trace Fossils: Concepts, Problems, Prospects. Elsevier, Amsterdam, pp. 110–134.
Masse, J.P., Fenerci-Masse, M., 2013. Drowning events, development and demise of carbonate platforms and controlling factors: the Late Barremian–Early Aptian record of Southeast France. Sediment. Geol. 298, 28–52.
Menegatti, A.P., Weissert, H., Brown, R.S., Tyson, R.V., Farrimond, P., Strasser, A., Caron, M., 1998. High-resolution δ13C stratigraphy through the early Aptian "Livello Selli" of the Alpine Tethys. Paleoceanography 13 (5), 530–545.
Millán, M.I., Weissert, H.J., Fernández-Mendiola, P.A., García-Mondéjar, J., 2009. Impact of Early Aptian carbon cycle perturbations on evolution of a marine shelf system in the Basque-Cantabrian Basin (Aralar, N Spain). Earth Planet. Sci. Lett. 287 (3–4), 392–401.
Murris, R.J., 1980. Middle East stratigraphic evolution and oil habitat. Am. Assoc. Pet. Geol. Bull. 64, 597–618.
Naafs, B.D.A., Pancost, R.D., 2016. Sea-surface temperature evolution across Aptian Oceanic Anoxic Event 1a. Geology 44, 959–962.
Naderi-Khujin, M., Seyrafian, A., Vaziri-Moghaddam, H., Tavakoli, V., 2016. A record of global change: OAE 1a in Dariyan shallow-water platform carbonates, southern Tethys, Persian Gulf, Iran. Facies 62 (4), 25.
Najarro, M., Rosales, I., Martín-Chivelet, J., 2011. Major palaeoenvironmental perturbation in an Early Aptian carbonate platform: prelude of the Oceanic Anoxic Event 1a? Sediment. Geol. 235 (1–2), 50–71.
Nozaki, Y., Zhang, J., Amakawa, H., 1997. The fractionation between Y and Ho in the marine environment. Earth Planet. Sci. Lett. 148 (1–2), 329–340.
Núñez-Useche, F., Barragán, R., Torres-Martínez, M.A., López-Zúñiga, P.A., Moreno-Bedmar, J.A., Chávez-Cabello, G., Chacon-Baca, E., 2020. Response of the western proto-North Atlantic margin to the early Aptian Oceanic Anoxic Event (OAE) 1a: an example from the Cupido platform margin-Gulf of Mexico, NE Mexico. Cretac. Res. 113, 104488.
Özer, S., Güngör, T., Sarı, B., Sagular, E.K., Görmüş, M., Özkar-Öngen, I., 2017. Cretaceous rudist-bearing platform carbonates from the Lycian Nappes (SW Turkey): Rudist associations and depositional setting. Cretac. Res. 79, 122–145.
Rameil, N., Immenhauser, A., Warrlich, G.M.D., Hillgärtner, H., Droste, H.J., 2010. Morphological patterns of Aptian Lithocodium-Bacinella geobodies relation to environment and scale. Sedimentology 57, 883–911.
Raven, M.J., van Buchem, F.S.P., Larsen, P.-H., Surlyk, F., Steinhardt, H., Cross, D., Klem, N., Emang, M., 2010. Late Aptian incised valleys and siliciclastic infill at the top of the Shu'aiba Formation (Block 5, offshore Qatar). In: van Buchem, F.S.P., AlHusseini, M.I., Maurer, F., Droste, H.J. (Eds.), Barremian-Aptian Stratigraphy and Hydrocarbon Habitat of the Eastern Arabian Plate, 2. GeoArabia Special Publication no. 4, pp. 469–502.
Ray, D.C., van Buchem, F.S.P., Baines, G., Davies, A., Greselle, B., Simmons, M.D., Robson, C., 2019. The magnitude and cause of short-term eustatic Cretaceous sea-level change: a synthesis. Earth Sci. Rev. 197, 102901.
Reershemius, T., Planavsky, N.J., 2021. What controls the duration and intensity of ocean anoxic events in the Paleozoic and the Mesozoic? Earth Sci. Rev. 221, 103787.
Roduit, N., . JMicroVision: Image analysis toolbox for measuring and quantifying components of high-definition images. Version 1.3.1. https://jmicrovision.github.io accessed 5 April.
Ross, D.J., Skelton, P.W., 1993. Rudist formation of the Cretaceous: a palaeoecological, sedimentological and stratigraphical review. In: Wright, V.P. (Ed.), Sedimentology Review/1. Blackwell, pp. 73–91.
Sames, B., Wagreich, M., Conrad, C.P., Iqbal, S., 2020. Aquifer-eustasy as the main driver of short-term sea-level fluctuations during Cretaceous hothouse climate phases. Geol. Soc. Lond. Spec. Publ. 498 (1), 9–38.
Schoepfer, S.D., Shen, J., Wei, H., Tyson, R.V., Ingall, E., Algeo, T.J., 2015. Total organic carbon, organic phosphorus, and biogenic barium fluxes as proxies for paleomarine productivity. Earth Sci. Rev. 149, 23–52.
Schroeder, R., van Buchem, F.S., Cherchi, A., Baghbani, D., Vincent, B., Immenhauser, A., Granier, B., 2010. Revised orbitolinid biostratigraphic zonation for the Barremian–Aptian of the eastern Arabian Plate and implications for regional stratigraphic correlations. In: van Buchem, F.S.P., AlHusseini, M.I., Maurer, F., Droste, H.J. (Eds.), Barremian-Aptian Stratigraphy and Hydrocarbon Habitat of the Eastern Arabian Plate, 2. GeoArabia Special Publication no. 4, pp. 49–96.
Scotese, C.R., 2021. An atlas of phanerozoic paleogeographic maps: the seas come in and the seas go out. Annu. Rev. Earth Planet. Sci. 49, 679–728.
Skelton, P.W., Gili, E., 2012. Rudists and carbonate platforms in the Aptian: a case study on biotic interactions with ocean chemistry and climate. Sedimentology 59 (1), 81–117.
Stein, M., Arnaud-Vanneau, A.N.N.I.E., Adatte, T., Fleitmann, D., Spangenberg, J.E., Foellmi, K.B., 2012. Palaeoenvironmental and palaeoecological change on the northern Tethyan carbonate platform during the Late Barremian to earliest Aptian. Sedimentology 59 (3), 939–963.
Steuber, T., Alsuwaidi, M., Hennhoefer, D., Sulieman, H., AlBlooshi, A., McAlpin, T.D., Shebl, H., 2022. Environmental change and carbon-cycle dynamics during the onset of Cretaceous oceanic anoxic event 1a from a carbonate-ramp depositional system, Abu Dhabi, UAE. Palaeogeogr. Palaeoclimatol. Palaeoecol. 601, 111086.
Taylor, S.R., McLennan, S.M., 1985. The Continental Crust: Its Composition and Evolution. Oxford Press, Blackwell, pp. 1–312.
Tribovillard, N., Algeo, T.J., Lyons, T., Riboulleau, A., 2006. Trace metals as paleoredox and paleoproductivity proxies. An update. Chem. Geol. 232, 12–32.
van Breugel, Y., Schouten, S., Tsikos, H., Erba, E., Price, G.D., Sinninghe Damsté, J.S., 2007. Synchronous negative carbon isotope shifts in marine and terrestrial biomarkers at the onset of the early Aptian oceanic anoxic event 1a: evidence for the release of 13C-depleted carbon into the atmosphere. Paleoceanography 22 (1), 1–13.
van Buchem, F.S., Al-Husseini, M.I., Maurer, F., Droste, H.J., Yose, L.A., 2010a. Sequence-stratigraphic synthesis of the Barremian–Aptian of the eastern Arabian Plate and implications for the petroleum habitat. In: van Buchem, F.S.P., AlHusseini, M.I., Maurer, F., Droste, H.J. (Eds.), Barremian-Aptian Stratigraphy and Hydrocarbon Habitat of the Eastern Arabian Plate, 2. GeoArabia Special Publication no. 4, pp. 9–48.
van Buchem, F.S.P., Baghbani, D., Bulot, L.G., Caron, M., Gaumet, F., Hosseini, A., Kayvani, F., Schroeder, R., Swennen, R., Vedrenne, V., Vincent, B., 2010b. Barremian—Lower Albian sequence stratigraphy of southwest Iran (Gadvan, Dariyan and Kazhdumi formations) and its comparison with Oman, Qatar and the United Arab Emirates. In: van Buchem, F.S.P., AlHusseini, M.I., Maurer, F., Droste, H.J. (Eds.), Barremian-Aptian Stratigraphy and Hydrocarbon Habitat of the Eastern Arabian Plate, 2. GeoArabia Special Publication no. 4, pp. 503–548.
van Buchem, F.S.P., Simmons, M.D., Droste, H.J., Davies, R.B., 2011. Late Aptian to Turonian stratigraphy of the eastern Arabian Plate – depositional sequences and lithostratigraphic nomenclature. Pet. Geosci. 17, 211–222.
Vilas, L., Masse, J.P., Arias, C., 1995. Orbitolina episodes in carbonate platform evolution: the early Aptian model from SE Spain. Palaeogeogr. Palaeoclimatol. Palaeoecol. 119 (1–2), 35–45.
Vincent, B., van Buchem, F.S.P., Bulot, L.G., Immenhauser, A., Caron, M., Baghbani, D., Huc, A.Y., 2010. Carbon-isotope stratigraphy, biostratigraphy and organic matter distribution in the Aptian e Lower Albian successions of Southwest Iran (Dariyan and Kazhdumi Formations). In: van Buchem, F.S.P., Al-Husseini, M.I., Maurer, F., Droste, H.J. (Eds.), BarremianeAptian Stratigraphy and Hydrocarbon Habitat of the Eastern Arabian Plate, GeoArabia Special Publication 4, vol. 2. GulfPetroLink, Bahrain, pp. 139–197.
Wang, C., Hu, X., Huang, Y., Wagreich, M., Scott, R., Hay, W., 2011. Cretaceous oceanic red beds as possible consequence of oceanic anoxic events. Sediment. Geol. 235 (1–2), 27–37.
Weissert, H., Lini, A., Foellmi, K.B., Kuhn, O., 1998. Correlation of Early Cretaceous carbon isotope stratigraphy and platform drowning events; a possible link? Palaeogeogr. Palaeoclimatol. Palaeoecol. 137, 189e203.
Wendler, J.E., Wendler, I., 2016. What drove sea-level fluctuations during the midCretaceous greenhouse climate? Palaeogeogr. Palaeoclimatol. Palaeoecol. 441, 412–419.

Westermann, S., Stein, M., Matera, V., Fiet, N., Fleitmann, D., Adatte, T., Föllmi, K.B., 2013. Rapid changes in the redox conditions of the western Tethys Ocean during the early Aptian oceanic anoxic event. Geochim. Cosmochim. Acta 121, 467–486.
Wissler, L., Weissert, H., Buonocunto, F.P., Ferreri, V., D'Argenio, B., 2004. Calibration of the Early Cretaceous time scale: A combined chemostratigraphic and cyclostratigraphic approach to the Barremian-Aptian interval Campania Apennines and southern Alps (Italy). In: D'Argenio, B., Fischer, A.G., Premoli Silva, I., Weissert, H., Ferreri, V. (Eds.), Cyclostratigraphy, Approaches and Case Histories. SEPM Special Publication, vol. 81, pp. 123–134.
Zhang, Z., Jansen, E., Sobolowski, S.P., Otterå, O.H., Ramstein, G., Guo, C., Nummelin, A., Bentsen, M., Dong, C.Y., Wang, X.J., Wang, H.J., Guo, Z., 2023. Atmospheric and oceanic circulation altered by global mean sea-level rise. Nat. Geosci. 1–7.
Ziegler, M.A., 2001. Late Permian to Holocene Paleofacies evolution of the. Arabian Plate and its hydrocarbon occurrences. GeoArabia 6, 445–504.